46th AIAA Aerospace Sciences Meeting and Exhibit
7 - 10 January 2008, Reno, Nevada

AIAA 2008-463

Influence of Space Weather on Aircraft Ionizing Radiation Exposure

Christopher J. Mertens[1], John W. Wilson[1], Steve R. Blattnig[1], Brian T. Kress[2], John W. Norbury[1], Michael J. Wiltberger[3], Stanley C. Solomon[3], W. Kent Tobiska[4], and John J. Murray[1]

[1]NASA Langley Research Center
Hampton, Virginia 23681

[2]Dartmouth College
Hanover, New Hampshire 03755

[3]High Altitude Observatory, National Center for Atmospheric Research
Boulder, Colorado 80301

Space Environment Technologies, Inc.
Pacific Palisades, California

Abstract

There is a growing concern for the health and safety of commercial aircrew and passengers due to their exposure to ionizing radiation with high linear energy transfer (LET), particularly at high latitudes. The International Commission of Radiobiological Protection (ICRP), the EPA, and the FAA consider the crews of commercial aircraft as radiation workers. During solar energetic particle (SEP) events, radiation exposure can exceed annual limits, and the number of serious health effects, especially to the unborn child of a pregnant air traveler, is expected to be quite high if precautions are not taken. There is a need for a capability to monitor the real-time radiation levels at commercial airline altitudes in order to: (1) provide a continuous assessment of the ionizing radiation field for tracking individual aircrew exposures levels, for the airlines and the FAA to develop policy and procedure for recommending aircrew radiation exposure limits and exposure mitigation; (2) provide time-critical data during SEP events for airline management and pilots to make decisions that balance the cost to flight path alterations against radiation exposure and health risks to passenger and crew; and (3) provide the airline industry with an archived database of radiation exposure levels for assessing the impact of ionizing radiation on the global air transportation system, especially in view of the current and future exponential increase in the number of polar routes.

Currently under development is the Nowcast of Atmospheric Ionizing Radiation for Aviation Safety (NAIRAS) model, which provides a global, data-driven, real-time, radiation dose prediction for archiving and assessing the biologically harmful radiation exposure levels at commercial airline altitudes. The NAIRAS model brings to bear the best available suite of Sun-Earth observations and models for simulating the atmospheric ionizing radiation environment. Observations are utilized from ground (neutron

monitors), from the atmosphere (the NCEP reanalysis), and from space (NASA/ACE and NOAA/GOES). Atmospheric observations provide the overhead shielding information and the ground- and space-based observations provide boundary conditions on the GCR and SEP energy flux distributions for transport and dosimetry simulations. Dose rates are calculated using the parametric AIR (Atmospheric Ionizing Radiation) model and the physics-based HZETRN (High Charge and Energy Transport) code. In this paper we present the concept and design of the NAIRAS model. Moreover, we show predictions of representative annual background exposure levels and radiation exposure levels during recent SEP events, with emphasis on high-latitude flight paths and polar routes.

1.0 Introduction

Atmospheric ionizing radiation is of interest to air transportation safety assessment because it's the primary source of human exposure to radiations with high linear energy transfer (LET). High-LET radiation is effective at producing chemically active radicals in biological tissues that alter the cell function or result in cell death. Consequently, there is increased concern for potential health outcomes among passengers and crew in commercial aviation [*Wilson et al.,* 2003a]. Atmospheric ionizing radiation is produced by extraterrestrial radiations incident on the Earth's atmosphere. The two sources of radiations are: (1) the ever-present, background galactic cosmic rays (GCR), with origins outside the solar system, and (2) transient solar energetic particles (SEP), which are associated with solar storm activity lasting several hours to days with widely varying intensity.

GCR consist of roughly 90% protons and 8% helium nuclei with the remainder being heavier nuclei and electrons [*Gaisser,* 1990]. When these particles penetrate the magnetic fields of the solar system and the Earth and reach the Earth's atmosphere, they collide with air molecules and create cascades of secondary radiations of every kind [*Reitz,* 1993]. The collisions are primarily due to Coulomb interactions of the GCR particle with orbital electrons of the air molecules, delivering small amounts of energy to the orbital electrons and leaving behind electron-ion pairs [*Wilson et al.,* 1991]. The ejected electrons usually have sufficient energy to undergo similar ionizing events. The cosmic ions lose a small fraction of their energy and must suffer many collisions before slowing down. On rare occasions the cosmic ion will collide with the nucleus of an air atom in which large energies are exchanged and the ion and nucleus are dramatically changed by the violence of the event. The remnant nucleus is highly disfigured and unstable, emitting further air nuclear constituents and decaying through the usual radioactivity channels [*Wilson et al.,* 1991]. One of the most important secondary particles created in GCR-air interactions is the neutron. Because of its charge neutrality, the neutron penetrates deep into the atmosphere, causing further ionization events along its path and contributing over half the atmospheric radiation exposure at typical commercial airline altitudes [*Wilson et al.,* 2003a]. Furthermore, neutron exposures pose a relatively high health risk, since the massive low-energy ions resulting from neutron interactions always produce copious ions in the struck cell and repair is less efficient for these events [*Wilson et al.,* 2000].

The intensity of the atmospheric radiations, composed of GCR primary and secondary particles, their energy distribution, and their effects on aircraft occupants vary with altitude, location in the geomagnetic field, and the time in the sun's magnetic activity (solar) cycle [*Reitz,* 1993; *Wilson,* 2000; and *Heinrich et al.,* 1999]. The atmosphere provides material shielding, which depends on the overhead atmospheric depth. The geomagnetic field provides a different kind of shielding, by deflecting low-momentum charged particles back to space. Because of the orientation of the geomagnetic field, which is predominately dipolar in nature, the polar regions and high latitudes are susceptible to penetrating GCR (and SEP) particles. At each geographic location, the minimum momentum per unit charge (magnetic rigidity) a vertically incident particle can have and still reach a given location above the earth is called the geomagnetic vertical cutoff rigidity. The local flux of incident GCR at a given time varies widely with geomagnetic location and the solar modulation level. When solar activity is high, GCR flux is low, and vice versa. The dynamical balance between outward convective flux of solar wind and the inward diffusive flux of GCR is responsible for the anti-correlation between the incident GCR and the level of solar activity [*Clem et al.,* 1996; *Parker,* 1965].

It is now generally understood that SEP events arise from coronal mass ejections (CME) from active regions of the solar surface [*Kahler,* 2001; *Wilson et al.,* 2005a]. The CME propagates through interplanetary space carrying along with it the local surface magnetic field frozen into the ejected mass. There is a transition (shock) region between the normal sectored magnetic structure of interplanetary space and the fields frozen into the ejected mass, where the interplanetary gas is accelerated forming the SEP. As the accelerated region passes an observation point, the flux intensity is observed to increase dramatically, and no upper limit in intensity is known within the shock region. The SEP energy spectrum obtained in the acceleration process is related to the plasma density and CME velocity. During a solar storm CME event, the number flux distribution incident at Earth's atmosphere is a combination of the GCR and SEP distributions. The SEP-air interaction mechanisms are the same as GCR-air interactions described above. The atmospheric radiations caused by a SEP also vary with altitude and geomagnetic field.

We are developing a prototype, global, data-driven, Nowcast of Atmospheric Ionizing Radiation for Aviation Safety (NAIRAS) model for calculating dose[1] equivalent[2] rates at commercial airline altitudes. The NAIRAS results provide a continuous assessment of the atmospheric ionizing radiation field needed for the commercial airlines to track individual aircrew radiation exposures levels, in order that the airlines and the FAA can develop policy and procedures for recommending aircrew radiation exposure limits and exposure mitigation. During SEP events, NAIRAS provides timely data output necessary for airline management and pilots to make critical decisions that balance cost to flight path alterations against radiation exposure and health risks to passenger and crew. NAIRAS will significantly enhance the NOAA/SEC decision support system since it

[1] Dose: Absorbed energy per mass (unit: 1 Gy = 6.24×10^{12} MeV kg^{-1})
[2] Dose equivalent: Sum of dose (Gy) of each radiation particle, with each particle weighted by a factor related to the potential for biological damaged (final unit: Sv)

currently does not provide observations, analysis, or forecasts of atmospheric ionizing radiation exposure.

The most significant and innovative features of the NAIRAS model are: (1) the atmospheric transport is simulated using HZETRN (High Charge and Energy Transport), a state-of-the-art, physics-based HZE+neutron+meson+muon transport code, which is (2) driven by real-time measurements of the solar-terrestrial environment – i.e., meteorological data of atmospheric density, observation-based models of GCR/SEP differential number flux spectrum (DNFS), and observation-based models of geomagnetic cutoff rigidity. Currently NOAA/SEC maintains a web site with space weather forecast products for the aviation community. The products include measurements of several space radiation environment parameters and a forecast on the likelihood and the expected level of space weather activity. The NOAA aviation products do not include the radiation fields that effect human health. The FAA's Civil Aerospace Medical Institute provides a web interface to the CARI-6 program. CARI-6 calculates effective dose rates of the GCR radiations for user-defined flight paths. The FAA web site does not maintain a real-time, global database. Furthermore, the CARI-6 calculations are based on average solar cycle modulation to the GCR background, which does not include SEP events or solar-storm perturbations to the geomagnetic cutoff rigidities.

There are no existing data or models that provide a comprehensive (i.e., comprehensive in terms of input observation data included and comprehensive in terms of the transport physics included in the real-time calculations), global, real-time assessment of the radiation fields that affect human health and safety. Thus, the NAIRAS model concept provides an atmospheric radiation exposure assessment that significantly extends current capabilities.

The NAIRAS model is highly relevant to a number NASA strategic goals and research objectives. NAIRAS is an application of Earth system science results (Earth's space and atmospheric observations and models) that greatly benefits society by providing critical data to quantify the health risk due to radiation exposure for commercial aircrew and passengers (NASA Strategic Subgoal 3A.7). The NAIRAS model also provides a tool for the aviation industry and the FAA to make informed decisions regarding radiation exposure mitigation procedures, during SEP events and for career planning purposes. Moreover, the NAIRAS model will document and quantify how human society is affected by solar variability (e.g., solar-geomagnetic storms and SEP events, and the solar-wind modulation of the GCR spectra) and magnetic fields (Earth's internal magnetic field and the interaction of the interplanetary magnetic field with Earth's magnetosphere) through their influence on the sources and variability of atmospheric ionizing radiation which can impact human health (NASA Strategic Subgoal 3B.2).

In section 2 we provide a narrative summary and salient results of progress made in FY2007 toward developing the NAIRAS model. Conclusions are presented in section 3.

2.0 Progress on NAIRAS Model Development

2.1 Ionizing Radiation Dosimetry Models

2.1.1 AIR Model

The Atmospheric Ionizing Radiation (AIR) model is a parametric model for predicting dose and dose equivalent. The development of the AIR model began decades ago at NASA Langley Research Center (LaRC) when the possibility of high-altitude supersonic commercial aviation was first seriously proposed [*Foelsche et al.,* 1961, 1974; and *Foelsche and Graul,* 1962]. The development effort included a comprehensive flight program in addition to theoretical investigations. More than 300 high-altitude aircraft flights and 25 balloon experiments were commissioned over most of the duration of solar cycle 20. The objective of the flight program was to study the background radiation levels over the solar cycle and to make measurements during SEP events. The LaRC flight package consisted of a 1-10 MeV neutron spectrometer, tissue equivalent ion chamber, and nuclear emulsion for nuclear reaction rates in tissue. Monte Carlo calculations [*Wilson et al.,* 1970; *Lambiotte et al.,* 1971] for incident GCR protons were used to extend the neutron spectrum to high energies. The measured data were combined with the theoretical calculations and integrated into the AIR model, parameterized by neutron monitor count rates, vertical geomagnetic cutoff rigidity, and atmospheric depth. The neutron flux (cm^{-2} sec^{-1}) component to the atmospheric radiations is converted to dose equivalent and total dose using 3.14 Sv cm^2 sec hr^{-1} and 0.5 Gy cm^2 sec hr^{-1}, respectively. The charged particle component to the atmospheric radiations is obtained from data taken by *Neher* [1961, 1967, 1971] and *Neher and Anderson* [1962] as compiled S. B. Curtis (Boeing 1969) and utilized by *Wallace and Sondhaus* [1978]. The charge particle atmospheric ionization rates are directly converted to dose equivalent and total dose using measurement data from the tissue equivalent ion chamber. Nuclear stars in tissue are estimated from the nuclear emulsion measurement data after subtraction of the neutron-induced stars [*Wilson et al.,* 1991].

More recent investigations of atmospheric ionizing radiation were also initiated and led by the LaRC team. These studies included an extensive flight package, which was a collaboration of fourteen institutions in five countries and consisted of eighteen instruments. New measurements [*Wilson et al.,* 2003a, *Goldhagan et al.,* 2002] were made which accompanied new advances in theoretical modeling [*Clem et al.,* 1996]. For example, improvements were made in the high-energy neutron spectrum from a combination of flight measurements and new theoretical calculations using the FLUKA transport code [*Clem et al.,* 2003]. Considerable progress was made in these recent LaRC studies, culminating in the AIR workshop [*Wilson et al.,* 2003a, 2005a].

The contribution of AIR to the overall NAIRAS model development is as follows. AIR will be used as an intermediate computational tool to develop the interface between neutron monitor data, the atmospheric depth data, and the geomagnetic cutoff model. This will allow simultaneous development of the integration of the components of the HZETRN code with the interface between HZETRN and the data-driven GCR/SEP models. Once the geomagnetic cutoff model and the atmospheric depth and neutron monitor data have been validated, verified, and benchmarked using the AIR model, these

models and data input will be integrated with HZETRN. A common I/O interface and data definitions will make this step effortless. Thus, HZETRN will eventually replace the AIR model for dose rate calculations, since a physics-based model is our overall objective. Thus, the purpose of the AIR model is to facilitate the integration, testing, and benchmarking of the components of the NAIRAS model, and to provide an empirical dosimetry code as a backup model and for rapid forecasting.

The remainder of section 2.1.1 describes the improvements and updates to the input data and models which parameterize the AIR model. Results from the updated version of AIR are also shown.

2.1.1.1 Neutron Monitor Data

The local flux of incident GCR at a given time varies widely with geomagnetic location (see next subsection) and solar modulation level. When solar activity is high, GCR flux is low, and vice versa. The dynamical balance between outward convective flux of solar wind and the inward diffusive flux of GCR is responsible for the anti-correlation between the incident GCR flux and the level of solar activity [*Clem et al.,* 1996; *Parker,* 1965]. Ground-based measurements of neutron counts rates provide a proxy for quantifying the influence of solar cycle modulation on the incident GCR flux. Figure 1 is representative of the anti-correlation between solar activity and GCR flux by comparing sun spot number with neutron count rates from the Climax neutron monitor site.

The AIR model uses ground-level neutron count rates as input data to parameterize solar cycle modulation effects. However, the AIR model parametric equations were fit to neutron count rates measured at the Deep River monitor site [*Wilson et al.,* 1991], which ceased operation in 1995. To increase the flexibility of the AIR model, and extend its usability beyond 1995, we have developed correlation relations between Deep River and other neutron monitor sites. Figure 2 shows count rates measured by Deep River and Climax. The count rates between the two monitors are highly correlated, as expected. The difference in magnitude in count rates measured by the two monitors is because they are stationed at different geomagnetic locations (see legend in Figure 2). In Figure 3 we show the fit derived between the Deep River neutron monitor and the Climax monitor. The fit was derived using count rates measured from 1958-1994, excluding the period 1963-1964 were there where obvious instrument problems at the Deep River site. Thus, the AIR model is extended beyond 1995 by using Climax neutron monitor count rates to derive "equivalent" count rates that would have been observed by Deep River using the fit equation shown in Figure 3. This technique will be utilized in real-time by the NAIRAS model using a global network of real-time neutron monitors [*Mavromichalaki et al*., 2006].

2.1.1.2 Vertical Geomagnetic Cutoff Rigidity

The AIR model is also parameterized by the vertical geomagnetic cutoff rigidity. The geomagnetic field provides a form of shielding by deflecting low-momentum charged particles back to space. At each geographic location, the minimum momentum per unit

charge (magnetic rigidity) a vertically incident particle can have and still reach a given location above the earth is called the vertical geomagnetic cutoff rigidity.

We have developed an in-house code to calculate global databases of quiescent vertical geomagnetic cutoff rigidities from numerical solutions of charged particle trajectories in the geomagnetic field, which is simulated using the International Geomagnetic Reference Field (IGRF) model [*Langlais and Mandea,* 2000], using the techniques advanced by *Shea and Smart* [1983] and *Smart and Shea* [2000, 2001]. The IGRF model includes dipolar and non-dipolar contributions to the geomagnetic field. Our starting point for developing the cutoff rigidity model is the charged particle trajectory code available from the NSSDC Space Physics ModelWeb (http://modelweb.gsfc.nasa.gov).

The baseline quiescent geomagnetic cutoff rigidity model consists of tabulated global databases of vertical cutoff rigidities calculated at yearly intervals using the charged particle trajectory simulations described above. The global cutoff rigidity databases can be computed up to five years beyond the current time period using secular trends in the derived spherical expansion coefficients of the internal geomagnetic field [*Langlais and Mandea*, 2000]. Figure 4 shows the global distribution of vertical geomagnetic cutoff rigidity computed for the 1996 epoch. A more sophisticated calculation of cutoff rigidity is required for magnetically disturbed periods. This topic is discussed in more detail in section 2.2.

2.1.1.3 Meteorological Fields

The atmosphere provides material shielding from incident cosmic rays, which depends on the overhead atmospheric depth. The AIR model is parameterized by atmospheric depth in units of g/cm^2. Sub-daily global atmospheric depth is determined from pressure versus geopotential height data and pressure versus temperature data derived from the National Centers for Environmental Prediction (NCEP) / National Center for Atmospheric Research (NCAR) Reanalysis 1 project [*Kalnay et al.,* 1996]. The NCEP/NCAR Reanalysis 1 project uses a state-of-the-art analysis/forecast system to perform data assimilation using past data from 1948 to the present. The data products are available 4x daily at 0, 6, 12, and 18 UT. The spatial coverage is 17 pressure levels in the vertical from approximately the surface (1000 hPa) to the middle stratosphere (10 hPa), while the horizontal grid is 2.5 degree x 2.5 degree covering 90N to 90S and 0E to 357.5E. The NCEP Reanalysis data are provided by the NOAA/OAR/ESRL PSD, Boulder, Colorado, USA, from their Web site at http://www.cdc.noaa.gov/, which can also be obtained via anonymous ftp.

Column abundance (or atmospheric depth in our units) is determined at each NCEP Reanalysis pressure surface by integrating atmospheric density over vertical height. Atmospheric depth (g/cm^2) is obtained at any specified commercial airline altitude by interpolating column densities at the NCEP Reanalysis pressure levels linearly in log pressure, using the geopotential height and temperature data at each NCEP pressure surface.

The data format for the NCEP Reanalysis 1 products is netcdf. We have developed Fortran routines to read the netcdf files and process the geopotential height and temperature data to produce sub-daily global distributions of atmospheric depth. As an example, Figure 5 shows the global distribution of NCEP Reanalysis pressure data at 12 km and at 17 UT on January 1, 1998 and on July 1, 1998. Figure 5 illustrates the seasonal variability in pressure at a given altitude due to the relative expansion and contraction of atmosphere, respectively, in the summer and winter hemispheres.

2.1.1.4 Global Distribution of Biological Dose

As previously stated, the input data to the parametric AIR model are neutron monitor count rates, vertical geomagnetic cutoff rigidity, and atmospheric depth. The input parameters capture the 3-D variability in atmospheric ionizing radiation exposure due to solar cycle modulation of, and momentum and atmospheric shielding of the incident GCR flux, respectively. We have updated the data input and interface to the AIR model so that AIR can be used in contemporary, real-time atmospheric dosimetry predictions. This activity facilitates the transition to the real-time, global physics-based atmospheric dosimetry model based on HZETRN. The three categories of input data required for the AIR model are also required input into HZETRN, as described in section 2.1.2.

Examples of dose rate calculations from the AIR model are shown in Figures 6-9. Figure 6 shows the global distribution of dose equivalent rates at 12 km for summer and winter seasons at solar maximum conditions for cycle 23. Figure 7 shows the northern hemisphere polar view of Figure 6. The North Atlantic flight corridor is one of the busiest in the world and it is among the most highly exposed routes in airline operations. Flights over Canada are among the most highly exposed. The exponential growth of polar routes from North American to Asia significantly increases radiation exposure for routine airline operations. Much of European flight is subject to somewhat lower exposure levels. For solar maximum conditions, aircrew can reach 60% to 70% of the annual recommend allowance in a 1000-hour block.

The season differences in Figures 6-7 are explained by the seasonal differences in atmospheric pressure shown in Figure 5. For example, the expansion of the atmosphere in the northern hemisphere summer, relative to the winter season, due to increased solar heating raises the pressure at 12 km. Elevated pressure at a given altitude increases the amount of overhead shielding of the GCR flux by the atmosphere. As a result, the radiation dose is less at a given altitude in summer compared to winter.

Figures 8-9 show the global distribution of dose equivalent rates at 12 km for summer and winter seasons at solar minimum conditions for cycle 23. Figure 9 is the northern hemisphere polar view of Figure 8. The seasonal differences are also evident at solar minimum. It is possible that aircrew flying the Northern Atlantic, Canadian, or polar routes can exceed the recommended allowable annual exposure levels in a 1000-hour block at solar minimum conditions. The occurrence of a SEP event could increase radiation exposure well over recommended and allowable levels.

2.1.2 HZETRN Code

The LaRC High Charge and Energy Transport (HZETRN) code has a long and successful history for rapid and accurate modeling of the particle radiation fields in the space environment. HZETRN is used to calculate dosimetric quantities on the International Space Station (ISS) and assess astronaut risk to space radiations, including realistic spacecraft and human geometry for final exposure evaluation. HZETRN is used as an engineering design tool for materials research for radiation shielding protection. Moreover, it is used to calculate HZE propagation through the Earth and Martian atmospheres, and to evaluate radiation exposures for epidemiological studies [*Wilson et al.,* 1986, 1987, 1997, 2003a, and references therein]. An extensive summary of verification and validation studies was recently reported by *Wilson et al.* [2005b].

The relevant HZE transport equations are the linear Boltzmann equations derived on the basis of conservation principles [*Wilson et al.,* 1991]. The transport equation for the flux density $\phi_j(\boldsymbol{x}, \boldsymbol{\Omega}, E)$ for particle type j is given by

$$\boldsymbol{\Omega} \cdot \nabla \phi_j(\boldsymbol{x},\boldsymbol{\Omega},E) = \sum \int \sigma_{jk}(\boldsymbol{\Omega},\boldsymbol{\Omega}',E,E')\, \phi_k(\boldsymbol{x},\boldsymbol{\Omega}',E')\, d\boldsymbol{\Omega}'\, dE' - \sigma_j(E)\, \phi_j(\boldsymbol{x},\boldsymbol{\Omega},E), \qquad (1)$$

where $\sigma_j(E)$ and $\sigma_{jk}(\boldsymbol{\Omega},\boldsymbol{\Omega}',E,E')$ are the target medium macroscopic cross sections. The $\sigma_{jk}(\boldsymbol{\Omega},\boldsymbol{\Omega}',E,E')$ represent all those processes by which type k particles moving in direction $\boldsymbol{\Omega}'$ with energy E' produce a type j particle in direction $\boldsymbol{\Omega}$ with energy E *(including radioactive decay processes).* The total cross section $\sigma_j(E)$ with the target medium for each particle type is

$$\sigma_j(E) = \sigma_{j,at}(E) + \sigma_{j,el}(E) + \sigma_{j,r}(E) \qquad (2)$$

where the first terms refers to collisions with atomic electrons, the second term refers to elastic ion-nuclear scattering, and the third contains all relevant nuclear reactions. The corresponding differential cross sections are similarly ordered.

Figures 10-12 provide heuristic illustrations of the effects of the three classes of interaction processes in (2) on the transport of GCR/SEP particles through the atmosphere. Collisions between incident GCR/SEP ions and atomic electrons of the target (neutral) atmospheric medium represent an energy loss channel (via ionization and/or excitation of the target atoms/molecules) for the incident GCR/SEP ions. After many such collisions, the ions will eventually come to rest. The distance an ion travels before coming to rest due to this energy loss mechanism is called the range of the ion. Figure 10 shows the range of various GCR ions versus the incident energy. Within a few percent, propagation distance in units of g/cm^2 is numerically equivalent to atmospheric pressure in units of hPa. Thus, the heaviest ions ($z > 10$ in Figure 10) are transported into the stratosphere before coming to rest due ionization of the neutral atmosphere. The lighter ions ($z < 10$ in Figure 10) can be transported into the troposphere before coming to rest.

The second interaction in (2) describes ion-nuclear Coulomb scattering between the incident ion and the neutral atmosphere. Figure 11 shows the characteristic scattering length for various GCR/SEP ions through the atmosphere. Ion-nuclear scattering becomes important at low energies. However, most GCR/SEP ions are stopped via ionization energy loss processes before a scattering event takes place. Multiple Coulomb scattering and coupling with ionization energy loss become important factors in the transport of ions within living tissue [*Mertens et al.,* 2007], which are related to the degree of biological damage inflicted on sensitive components within the living cell.

The probability of a nuclear reaction is a function of the third interaction cross section in (2), and is a quantity that explicitly appears in the solution of the Boltzmann transport equation in (1). Figure 12 shows the probability of a nuclear reaction versus energy for GCR/SEP ions incident on the atmosphere. The high-energy GCR particles are assured of undergoing several nuclear reactions before coming to rest in Earth's atmosphere. The high-energy nuclear reactions are accompanied by large energy exchanges which fragment both the projectile and target nuclei into lighter secondary particles.

The solution of (1) involves hundreds of multidimensional integral-differential equations, which are coupled together by thousands of cross terms and must be solved self-consistently subject to boundary conditions ultimately related to the external environment. Neutrons are not subject to electromagnetic interactions (i.e., the first two terms in (2)) and different approaches were developed to solve the neutron transport equations [*Clowdsley et al.,* 2000, 2002]. Details of all the analytical and computational solution approaches in HZETRN are given by *Wilson et al.* [2004, 1997, 1991, 1987, 1986, and references therein].

Recently, *Blattnig et al.* [2004, 2005] developed a meson-muon transport code, called MESTRN, including nuclear electromagnetic cascade effects. Muons dominate the radiation on the ground, but are much less important at the top of the atmosphere. Their greatest contribution at commercial airline altitudes is likely through electromagnetic cascade processes. Thus, we will integrate MESTRN with HZETRN and assess the meson-muon contribution to atmosphere radiation exposure. The abundance of ground-based muon measurements provides an indispensable source of indirect checks on the ion and neutron transport.

The HZETRN component of the NAIRAS model will include the transport of HZE+neutrons+mesons+muons+electromagnetic cascade particles through the atmosphere. This represents the most comprehensive physics-based atmospheric radiation transport code to date.

2.1.2.1 Nuclear Databases

Recent improvements have been made in the parameterization of two categories of nuclear cross sections which are important for GCR/SEP atmospheric transport. Recall that the nuclear cross sections correspond to the third interaction term in (2). The first cross section category that has been improved is neutron-nucleus elastic differential cross

sections. Since neutron radiation is a major contributor to aircraft GCR/SEP exposure, and since neutron exposure poses a relatively high health risk, it is important to continue to improve upon the theoretical understanding and parameterization of nuclear reactions related to atmospheric neutron transport. The neutron-nucleus elastic differential cross sections were updated via improvements in the total nucleon-nucleon cross sections, which are input data in the parameterization of the neutron-nucleus elastic differential cross sections. Although the global fits in the current total nucleon-nucleon cross section parameterization in HZETRN were generally quite good, there were remaining discrepancies in the spectral region of maximum GRC intensity. These discrepancies have been significantly reduced by an improved parameterization of the total nucleon-nucleon cross sections [*Norbury,* 2007a], as shown in Figures 13-14 for proton-proton and proton-neutron collisions, respectively. Significant improvements are evident in the region of maximum GCR spectrum (i.e., ~ 500-1000 MeV/nucleon, see Figure 17).

Hadron production at intermediate energies from nucleus-nucleus interactions is important for space and atmospheric radiation transport. The intermediate energy regime is where the cosmic ray spectra peak in intensity. However, theoretical methods work best at low energies, where non-relativistic theory is valid, or at high energies where ultrarelativistic approximations can be applied. Recent efforts have extended the current high energy parameterizations of hadron production from nucleon-nucleon collisions to include arbitrary nucleus-nucleus collisions. Moreover, the hadron production cross sections have been extended to intermediate energies using a simple thermal model parameterization [*Norbury and Blattnig*, 2007b]. Figures 15-16 show the momentum spectrum of the differential π^- production cross section at various scattering angles in laboratory frame from collision of argon (Ar) with potassium chloride (KCl). The agreement between the theoretical hadron production cross sections and cross sections obtained from beam experiments has been significantly improved compared to previous cross section parameterizations [see *Norbury and Blattnig*, 2007b].

2.1.2.2 GCR Model

The solutions to the Boltzmann transport equation (1) are unique in any convex region for which the inbound flux of each particle type is specified everywhere on the bounding surface [*Wilson et al.,* 1997]. For real-time transport calculations of GCR particles, we use the *Badhwar and O'Neill* [1996, 1994, 1993, 1992, 1991] model to specify the incident GCR DNFS at the top of the atmosphere. The recently updated version of the GCR model is driven by ground-based neutron monitor count rate measurements from the Climate neutron monitor site.

The GCR DNFS incident on Earth's atmosphere is predicted in the Badhwar and O'Neill model by propagating the local interstellar spectrum (LIS) of each element to 1 A.U. by solving a steady-state, spherically symmetric Fokker-Planck transport equation, which accounts for diffusion, convection, and adiabatic deceleration of cosmic rays entering the heliosphere [*Parker*, 1965]. The functional form of the diffusion coefficient is taken to be

$$k(r,t) = (k_0 / V_{SW})\beta R\left[1+\left(r / r_0\right)^2\right] / \Phi(t), \tag{3}$$

where V_{SW} is the solar wind speed (nominally set to 400 km/s for all time t), r is the distance from the sun in A.U., t is time in years, k_0 and r_0 are constants, β is the particle's speed relative to the speed of light, R is the particle's magnetic rigidity in MV, and Φ is the so-called solar modulation parameter. Thus, the time-dependent behavior of the GCR flux, due to the level of solar activity, is completely embedded into the solar modulation parameter, which is physically related to the energy and rigidity an interstellar nuclei must have in order to propagate through the heliosphere to the radius in question. The solar modulation parameter is determined by fitting the solution of the Fokker-Planck equation for a specified element to corresponding spectral flux measurements throughout the solar cycle, as described in the paragraph below.

For a fixed parameterization of the LIS, the solar modulation parameter in (3) (i.e., $\Phi(t)$) was determined by fitting the solution of the steady-state Fokker-Planck equation for oxygen nuclei to measurements of DNFS. For energies below roughly 1 GeV (i.e. ~ 50-500 MeV/nucleon), the measurement data were obtained from the Cosmic Ray Isotope Spectrometer (CRIS) instrument on the NASA Advanced Composition Explorer (ACE) satellite. For higher energies (1-35 GeV), the model was fit to data from the C2 instrument on the NASA High Energy Astrophysical Observatory (HEAO-3) satellite [*Englemann et al.*, 1990].

It is difficult to distinguish the GCR and solar components for protons and alpha spectra observed by CRIS. Fortunately, *Lopate* [2004] provided an extensive database of quiescent proton and alpha specta from IMP-8 measurements. Thus, the proton and alpha spectra in the Badhwar and O'Neill model were fit to IMP-8 data. The high energy proton and alpha spectra were fit to the balloon-borne Isotope Matter-Antimatter Experiment (IMAX) measurements [*Menn et al*., 2000].

Once the solar modulation parameter was derived based on the NASA/ACE/CRIS oxygen spectra, as described in the above paragraph, the LIS for the remaining elements (i.e., lithium (Z=3) through nickel (Z=28)) were similarly determined by fitting the solutions of the Fokker-Planck equation to the CRIS DNFS measurements. A simple power law form of the differential LIS was assumed,

$$j_{\mathrm{LIS}}(E) = j_0 \beta^{\delta} \left(E + E_0\right)^{-\gamma}, \tag{4}$$

where E is the particle kinetic energy per nucleon and E_0 is the rest mass energy per nucleon (938 MeV/n). The free parameters (γ,δ, and j_0) were determined from the fit of the GCR model to the CRIS measurements.

The Badhwar and O'Neill GCR model was extended beyond the time period of the ACE/CRIS measurements in the following way. First, the solar modulation parameter was alternatively derived from the IMP-8 channel 7 (z >8, high energy) measurements over three solar cycles from 1973 through 2001, and was calibrated against the solar modulation parameter derived from ACE/CRIS for the period of data overlap (1997.6 to 2001.8). GCR flux comparisons using both sets of solar modulation parameters correlated

to within 98.9%. Next, linear fit coefficients were derived between the IMP-8 solar modulation parameter and Climax neutron monitor count rates from 1973-2001. The solar modulation parameter computed using the Climax neutron count rates correlated with the solar modulation parameter derived from IMP-8 data within 97%. Linear fits were derived for the three polarity states of the solar magnetic field: (1) positive solar cycle (outward field), (2) negative solar cycle (inward field), and (3) transition state (intermediate between positive and negative polarities with a high degree of modulation). The linear fit coefficients for the three polarity states are given in Table 1.

To capture the real-time modulation of the GCR DNFS by the solar wind (or solar activity), Climax neutron count rates will be cross correlated with count rates observed from the world-wide network of real-time neutron count monitors, as described in section 2.1.1.1. Real-time neutron monitor data will be obtained from approximately 13 different sites, such as IZMIRAN (Moscow, Russia), YAKUTSK (Russia), and LOMNICKY (Slovakia).

Figure 17 shows GCR DNFS predicted by the Badhwar and O'Neill model for representative elemental nuclei important for space and atmospheric radiation transport. The red line is the LIS. One can clearly see the influence of the solar activity cycle on the modulation of the GCR spectrum. Solar minimum and solar maximum conditions for cycle 23 are denoted by the green and blue lines in Figure 17, respectively. The GCR DNFS predicted by the Badhwar and O'Neill model provide the boundary specification of inbound particle flux for each GCR nuclei for the atmospheric radiation transport and dosimetry calculations by HZETRN.

2.1.2.3 SEP Model

SEP proton and alpha DNFS will be obtained in real-time from NOAA's Geostationary Operational Environmental Satellite (GOES) Space Environment Monitor (SEM) measurements. The Energetic Particle Sensor (EPS) and the High Energy Proton and Alpha Detector (HEPAD) sensors on GOES/SEM measure energetic differential proton and alpha flux. EPS provides seven-channels of differential proton flux from 0.8 to 500 MeV and five-channels of differential alpha flux from 4 to 250 MeV per nucleon. HEPAD extends the EPS energy ranges to greater than 700 MeV for protons and greater than 3400 MeV per nucleon for alpha particles. However, we exclude measurements for energies less than 5 MeV for both proton and alpha particles since there is greater possibility that the magnetosphere may be the source of these particles.

The SEP DNFS is assumed to be represented by a double power law form. The low energy portion of the spectrum is represented by the *Ellison and Ramat*y [1985] expression:

$$dJ / dE = KE^{-\gamma} \exp(-E / E_0), \tag{5}$$

where J is the particle flux (cm^{-2} sr^{-1} s^{-1}), E is kinetic energy per nucleon (MeV/n); K, E_0, and γ are constants to be determined. The above spectrum has a power law shape at low

energies, as expected from shock acceleration, with an exponential rollover at high energies, which may be related to the finite radius of the shock or the time available for accelerating particles to high energy. *Mewaldt et al.* [2005] found that the Ellison-Ramaty form failed to fit the highest energy portion of the spectrum, as determined by particle flux measurements during the Halloween (October-November) 2003 superstorm event. They found that a double power law representation significantly improved the fit to the measured spectra. By requiring that the two functional forms of the DNFS are equal in magnitude and in slope at the energy where the two functions merge, the following form can be derived:

$$\begin{aligned} dJ/dE &= CE^{-\gamma_a}\exp(-E/E_0) \text{ for } E \le (\gamma_b - \gamma_a)E_0 \\ dJ/dE &= CE^{-\gamma_b}\left\{\left[(\gamma_b - \gamma_a)E_0\right]^{(\gamma_b-\gamma_a)}\exp(\gamma_a - \gamma_b)\right\} \text{ for } E > (\gamma_b - \gamma_a)E_0, \end{aligned} \tag{6}$$

where γ_a is the low-energy power law slope and γ_b is the high-energy power law slope, and E and E0 are measured in kinetic energy per nucleon (MeV/n).

We assume that both the proton and alpha SEP DNFS are represented by the double power law form in (6). The constants C, γ_a, γ_b, and E_0 are determined by a nonlinear least-square fit to the measured spectra. Table 2 lists the GOES/SEM EPS and HEPAD proton and alpha DNFS channels used in the spectral fitting procedure. Note that some of the proton spectral channels listed in Table 2 are derived from the integral flux channels and are not independent measurements with respect to the differential flux channels.

The Halloween 2003 superstorm event marked some of the largest solar activity in the history of the space age. Figure 18 shows GOES EPS measurements of integral proton flux from October 1 through November 30, 2003. Figure 19 shows the proton DNFS derived from satellite particle flux measurements for five SEP events during the Halloween superstorm, as analyzed by *Mewaldt et al.* [2005]. These events are more intense than some of the historical SEP spectra that are commonly used in space weather engineering design and radiation risk studies, as shown in Figure 20. The Halloween 2003 SEP spectra will serve as benchmark studies of the impact of SEP events on atmospheric ionizing radiation and radiation exposure.

2.1.2.4 Vertical Geomagnetic Cutoff Rigidity

The geomagnetic cutoff rigidity also functions as a canonical variable for specifying the minimum access energy of incident GCR/SEP particles for transport through the atmosphere. Once the cutoff rigidity is known, the minimum access energy is determined for each incident particle of charge number Z and mass number A through the relativistic energy equation, such that

$$E = \left[\sqrt{R^2\left(Z/A\cdot \text{amu}\cdot c^2\right)^2 + 1} - 1\right]\cdot \text{amu}\cdot c^2. \tag{7}$$

In the above equation, E is kinetic energy per nucleon (MeV/n), R is geomagnetic cutoff rigidity (MV), c is the speed of light in vacuum, and amu = 931.5 MeV/c^2 (atomic mass unit).

Numerical instabilities in HZETRN which prohibited a sharp energy cutoff have been corrected. Figures 21 and 22 show the effect of geomagnetic cutoff rigidity on the atmospheric transport of an SEP spectrum. The incident SEP spectrum corresponds to event 2 (10/28 (1100 UT) – 10/29 (2000 UT) from the Halloween 2003 storm shown in Figure 19. Proton and neutron flux are shown at various atmospheric depths. Within a few percent, atmospheric depth in units of g/cm^2 is numerically equivalent to atmospheric pressure in units of hPa (or mb). Figure 21 shows the particle flux for zero geomagnetic cutoff rigidity, which is representative of geomagnetic conditions of the polar region. Figure 22 shows the particle flux for a 1 GV cutoff rigidity, which is characteristic of the cutoff rigidity along the North Atlantic flight corridor and some portions of flight paths from North America to Asia. Even though a significant fraction of the incident SEP spectrum has been "filtered" by the geomagnetic field, as clearly indicated in Figure 22, a significant build up of secondary particles ensue. Figures 23 and 24 show similar plots for the GCR spectra. GCR spectra for zero geomagnetic cutoff rigidity are shown in Figure 23, while Figure 24 shows GCR spectra for a 1 GV cutoff rigidity.

2.1.2.5 Meteorological Fields

HZETRN transports the incident particle spectra and dosimetric quantities as a function of propagation distance (in units of g/cm^2) through the intervening media. Once the dosimetric quantities are computed on a grid of atmospheric depth (in g/cm^2), they are mapped to an altitude grid using NCEP Reanalysis 1 geopotential height data described in section 2.1.1.3. The left panel in Figure 25 shows the dose rate in air as a function of atmospheric depth. The dose rate was computed for yearly-averaged incident GCR flux in 1996, which represents solar minimum conditions for cycle 23. The geomagnetic cutoff rigidity was taken to be 1 GV. Under quiescent conditions, the geographic location at 60N, 350E is characterized by a 1 GV geomagnetic cutoff rigidity at 20 km, for example. We use this geographic location to illustrate the mapping of dose as function of atmospheric depth to altitude using the NCEP geopotential height data. The right panel in Figure 25 shows the altitude profile of atmospheric dose on January 1, 1996 at 17:00 UT corresponding to the dose versus depth profile in the left panel.

2.1.2.6 Global Distribution of Atmospheric Dose

The goal is to predict the global distribution of atmospheric ionizing radiation dose at a one-hour time cadence using the data-driven, physics-based HZETRN model for transport and dosimetry calculations. The one-hour averaged neutron count rate, derived from one of the 13 real-time neutron monitor sites described in section 2.1.2.2, is used to predict the incident GCR spectrum using the Badhwar and O'Neill GCR model. During an SEP event, the one-hour averaged proton and alpha spectral measurements from NOAA/GOES will be used to fit the double-power law analytical spectrum described in section 2.1.2.3. For SEP events, a global grid of geomagnetic cutoff rigidities will be

computed using real-time observations from NASA/ACE solar wind and IMF measurements. Once the incident GCR/SEP spectra and cutoff rigidities have been specified, HZETRN will compute the atmospheric dose rates for one vertical ray path from the top of atmosphere to the surface as a function of atmospheric depth and cutoff rigidity. The global distribution of atmospheric dose will be obtained via interpolation in geomagnetic cutoff rigidity (specified at each geo-location) and mapping from atmospheric depth to altitude at each geo-location using real-time NCEP Reanalysis 1 geopotential height data. The directional dependent flux distribution for evaluating dose within the aircraft will be obtained assuming plane-parallel geometry, scaling the slant path by the secant of the vertical ray path, and interpolating within the array of vertical ray path atmospheric dose rates.

Each of the components described in the above paragraph for predicting the real-time global distribution of atmospheric radiation dose have been developed. The remaining task in to integrate and automate the components.

Figure 26 shows air dose rates for various geomagnetic cutoff rigidities for one of the five SEP events analyzed during the Halloween 2003 superstorm event (see Figure 19 for SEP spectra). The results shown in this figure indicate that SEP events pose a significant increase in ionizing radiation exposure for geo-locations with a cutoff rigidity below about 1 GV. Thus, international flights along the North Atlantic corridor, Canadian routes, and polar routes from North America into Asia can expect significant exposure to biologically harmful radiation if mitigation procedures are not made.

Figure 27 shows background GCR air dose rates at solar cycle 23 minimum (1996) for various cutoff rigidities. Due to the high-energy component and soft spectra shape of the GCR spectrum, the geomagnetic cutoff rigidity does not have as strong a filtering effect on the GCR spectrum per increase in rigidity as compared to the SEP spectrum in the previous figure.

2.2 Influence of Magnetospheric Current Sources

The global grid of vertical cutoff rigidities described in section 2.1.1.2 predicts the cutoff rigidity during quiescent conditions. The parameter that accounts for the main perturbations in the cutoff rigidities due to geomagnetic storms is a change in the horizontal component of the geomagnetic field at the magnetic equator. The horizontal component of the magnetic field, in turn, is perturbed largely by an intensification of the ring current [*Kuhn et al.,* 1965; *Wilson et al.,* 1991, 2003; *De Angelis et al.,* 2003]. Real-time perturbations to the horizontal component of the geomagnetic field can be modeled by driving the T96, T01, or T05 magnetospheric magnetic field models [*Tsyganenko et al.,* 1989, 2002, 2005] with measurements of the interplanetary magnetic field (IMF) and solar wind dynamic pressure, among other parameters, from the NASA/ACE satellite and Dst-index obtained from NOAA/SEC.

A more sophisticated calculation of cutoff rigidity during magnetically disturbed periods can be provided by the use of a full numerical simulation using the coupled

magnetosphere-ionosphere-thermosphere (CMIT) model [*Wiltberger et al.,* 2004]. This model combines the Lyon-Fedder-Mobarry MHD simulation of magnetospheric dynamics [*Lyon et al.,* 2004] with the Thermosphere-Ionosphere Nested Grid (TING) model for the upper atmosphere and ionosphere [*Wang et al.,* 1999]. CMIT can be run using solar wind and IMF data such as is available in near-real-time from the NASA/ACE spacecraft. The Center for Integrated Space-weather Modeling (CISM) [*Luhmann et al.,* 2004; *Spence et al.,* 2004] is developing a comprehensive model for studying the interaction of solar energetic particles with the magnetosphere using a 3D Lorentz integration of SEP trajectories in electric and magnetic fields taken from the CMIT model [*Kress et al.,* 2005, 2004; *Hudson et al.,* 2004; *Weygand and Raeder,* 2005]. These simulations can be employed to obtain a detailed morphology of the cutoff rigidity using a dynamic magnetic field which results from geomagnetic activity that typically accompanies these events.

We are currently using both of the above magnetospheric magnetic field models – i.e., the empirical T05 model and the physics-based fields computed by the CMIT/LFM/MHD magnetospheric model – to assess the impact of magnetospheric current sources on the geomagnetic cutoff rigidity, both under quiet and magnetically disturbed conditions. Figure 28 shows the difference in computed vertical geomagnetic cutoff rigidities using the IGRF model (i.e., no magnetospheric effects) versus using the T05 model. The differences are shown in units of rigidity for IGRF-T05. The T05 model was run for solar wind and IMF conditions at 22:00 UT on September 24, 1998, representative of quiescent conditions. Using the IGRF model only, the cutoff rigidities are underestimated. There are isolated regions where the differences are ~ 1 GV or greater, but the most noticeable feature is the large band of ~ 0.7 GV differences displaced above and below the magnetic equator. Even under quiescent conditions, the diamagnetic perturbation to the internal geomagnetic field (IGRF model) due to the ring current, which is accounted for in the T05 model, has a noticeable effect on the vertical cutoff rigidities.

The overestimation in geomagnetic cutoff rigidity by not including magnetospheric current sources such as the ring current, as shown in Figure 28, causes an underestimation of biological dose. Figure 29 shows the corresponding difference in annual dose equivalent rate due to the differences in vertical cutoff rigidity shown in Figure 28. The dose can be underestimated by up to 1.3 mSv/1000 hours. This underestimation is not too significant in terms of annual exposure level. However, during magnetically disturbed conditions, the suppression of the cutoff rigidity is much greater and adds to this background suppression of cutoff rigidity during quiescent conditions. This cumulative suppression of cutoff rigidity during geomagnetic storms can significantly increase radiation dose levels.

Figure 30 shows the magnetic field lines computed by the two magnetospheric models used in our studies. The top panel is field lines computed by the CMIT/LFM/MHD model. The bottom panel shows field lines computed by the T05 model. The field line tracing shown in Figure 30 is in the meridional (x-z) plane in solar-magnetic coordinates. The sun is directed along the positive x-axis and the magnetic dipole moment is along the z-axis. The field lines computed by both models represent the snap shot of the

magnetosphere at 23:00 UT on September 24, 1998, prior to the storm event. The T05 model includes the effects of the ring current on the magnetospheric magnetic field while the CMIT/LFM/MHD model does not (see difference in field lines in the magnetotail region in Figure 30). Thus, the T05 model provides a better estimate of the cutoff rigidity, as described in more detail below.

Figures 31 and 32 show geomagnetic cutoff rigidities computed during the September 1998 storm period. Maximum solar wind dynamic pressure and minimum Dst-index (corresponding to largest perturbation in the horizontal component of the geomagnetic field) occur at 06:32 UT on September 25, 1998. Figure 31 shows contours of cutoff rigidities using T05 to simulate the magnetic field. Also shown in this figure is measured cutoff rigidity determined by SAMPEX observations for the closest time coincidence to the simulated snap shot. The comparison is good: the observed cutoff rigidity by SAMPEX differs by no more than one degree in latitude from the corresponding cutoff rigidity contour computed using the T05 model. Figure 32 shows the difference in geomagnetic cutoff rigidity before (22: 00 UT on September 24, 1998) and during (06:32UT on September 25, 1998) the storm, as computed using the T05 model. The largest differences occur in a latitude band displaced above and below the magnetic equator. The storm-time suppression of the cutoff rigidity can be as much as ~ 1 GV, and occurs over the heavily traveled airspace for international commercial routes from North America into Asia and Europe. Combine this storm-time suppression of the geomagnetic cutoff rigidity with the effect of the quiet time magnetosphere discussed above; the result is a ~ 2 GV suppression of cutoff rigidity due to magnetospheric current source during solar-geomagnetic storms. A ~1-2 GV suppression in cutoff rigidity can translate into a significant increase in radiation dose at mid- to high-latitudes.

Figures 33 and 34 show September 1998 cutoff rigidities computed using the CMIT/LFM/MHD model. The storm-time contours of cutoff rigidities in Figure 3 were computed at 06:32 UT on September 25, 1998, the same time as shown in Figure 31. Notice that the comparison of CMIT/LFM/MHD cutoff rigidity simulations with SAMPEX observations is not nearly as good as the comparison between SAMPEX and the cutoff rigidity computed using the T05 model. The reason for the larger discrepancy between modeled and observed cutoff rigidity for the CMIT/LFM/MHD magnetospheric model is due to the lack of coupling to ring current dynamics. Figure 34 shows the difference in simulated cutoff rigidity between storm and quiet conditions using the CMIT/LFM/MHD model. The storm-quiet differences in cutoff rigidity are much smaller compared to the differences shown if Figure 32, which is again attributed to the lack of ring current dynamics included in the CMIT.LFM/MHD model.

3.0 Conclusions

Significant progress has been made toward developing the NAIRAS concept. The parametric AIR has been updated to include state-of-the-art capability in specifying the solar modulation of background GCR exposure, the vertical geomagnetic cutoff rigidity, and the mapping of atmospheric depth to altitude scale. The AIR model can be used in real-time to predict background atmospheric ionizing radiation dose rates. A reanalysis of

the solar maximum and solar minimum background exposures for summer and winter seasons have been made.

HZETRN has been configured for real-time atmospheric transport of incident GCR/SEP spectra and dosimetric calculations. The development of the interface between HZETRN and the data-driven input parameters has progressed significantly. The input parameters for HZETRN are the same as needed by the AIR model described in the proceeding paragraph. Critical improvements to nuclear cross sections have been made which impact atmospheric neutron and meson-muon transport. Preliminary analysis of background radiation dose rates and atmospheric dose for SEP events during the Halloween 2003 superstorm event have been made.

Progress has been made in understanding the influence of magnetospheric effects on geomagnetic cutoff rigidities, and their subsequent impact on atmospheric dose. Both quiescent and storm events has been analyzed. This work provides critical guidance for developing an accurate and computationally feasible cutoff rigidity model during solar-geomagnetic storms.

Future efforts will be concentrated in four major areas. The first area is model integration. We will continue to integrate the real-time input models and data source with HZETRN, and complete the input data integration for the parametric AIR model. Furthermore, we will integrate MESTRN and electromagnetic cascade interactions and transport with HZETRN. The second area of effort is transport physics and interactions. More work is needed to improve the forward and backward neutron transport and hadron production cross sections for HZETRN. The third area of effort is magnetospheric effects on cutoff rigidities. We will continue to characterize these magnetospheric effects during both quiescent and storm conditions. Continued investigation in this area is needed in order to develop the requirements and strategy for real-time geomagnetic cutoff rigidity storm model. The fourth area is verification and validation. We will assemble ground-level, atmospheric, and space-based measurements to characterize and reduce the uncertainties in each component of the NAIRAS model.

References

Badhwar, G. D., and P. M. O'Neill, Galactic cosmic radiation model and its applications, *Adv. Space Res.,* **17**, 7-17, 1996.

Badhwar, G. D., and P. M. O'Neill, Long term modulation of galactic cosmic radiation and its model for space exploration, *Adv. Space Res.*, **14**, 749-757, 1994.

Badhwar, G. D., and P. M. O'Neill, Time lag of twenty-two year solar modulation, *Proc. 23rd Int'l Cosmic Ray Conf. (Calgary)*, **3**, 535-539, 1993.

Badhwar, G. D., and P. M. O'Neill, An improved model of galactic cosmic radiation for space exploration missions, *Nuclear Tracks Radiat. Meas.*, **20**, 403-410, 1992.

Badhwar, G. D., and P. M. O'Neill, An improved model of galactic cosmic radiation for space exploration missions, *Proc. 22nd Int'l Cosmic Ray Conf. (Dublin)*, **OG-5.2-13**, 643-646, 1991.

Blattnig, S. R., G. De Angelis, F. F. Badavi, R. B. Norman, and J. W. Norbury, Preliminary analysis of pion and muon radiations on Mars, submitted to *Advances in Space Research*, 2005.

Blattnig, S. R., J. W. Norbury, R. B. Norman, J. W. Wilson, R. C. Singleterry, R. K. Tripathi, MESTRN: A Deterministic Meson-Muon Transport Code for Space Radiations, *NASA/TP-2004-212995*, 2004.

Clowdsley, M. S., et al., *Shuttle Induced Neutron Environment: Computational Requirements and Validation,* International Conference on Environment Systems, SAE 2002-01-2460, 2002.

Clowdsley, M. S., et al., A comparison of the multigroup and collocation methods for solving the low-energy neutron Boltzmann equation, *Can. J. Phys.,* **78***, 45-56,* 2000.

Clem, J. M., G. De Angelis, P. Goldhagan, and J. W. Wilson, Preliminary validation of computational procedures for a new atmospheric ionizing radiation (AIR) model, *Adv. Space Res.,* **32(1)**, 27-33, 2003.

Clem, J., D. P. Clements, J. Esposito, P. Evenson, D. Huber, J. L'Heureux, P. Meyer, and C. Constantin, Solar modulation of cosmic electrons, *Astrophys. J.,* 464, 507, 1996.

De Angelis, G., J. M. Clem, P. E. Goldhagen, and J. W. Wilson, A new dynamical ionizing radiation (AIR) model for epidemiological studies, *Adv. Space Res.,* **32(1)**, 17-26, 2003.

Ellison, D. C., and R. Ramaty, Shock acceleration of electrons and ions in solar flares, *Astrophys. J.,* **298**, 400-408, 1985.

Engelmann, J. J., P. Ferrando, A. Soutoul, P. Goret, E. Juliusson, L. Koch-Miramond, N. Lund, P. Masse, B. Peters, N. Petrou, and I. L. Rasmussen, Charge composition and energy spectra of cosmic-ray nuclei for elements from Be to Ni. Results from HEAO-3-C2, *Astron. Astrophys.*, **233**, 96-111, 1990.

Foelsche, T., R. B. Mendell, J. W. Wilson, and R. R. Adams, Measured and calculated neutron spectra and dose equivalent rates at high altitudes: Relevence to SST operations and space research, *NASA TN D-7715,* 1974.

Foelsche, T., Radiation Exposure in Supersonic Transports, NASA TN D-1383, 1961.

Foelsche, T., and E. H. Graul, Radiation exposure in supersonic transports, *Atompraxis*, **8**, 365-380, 1962.

Gaisser, T., *Cosmic Rays and Particle Physics,* Cambridge University Press, 1990.

Goldhagan, P., M. Reginatto, T. Kniss, J. W. Wilson, R. C. Singleterry, I. W. Jones, and W. Van Steveninck, Measurement of the energy spectrum of cosmic-ray induced neutrons aboeard an ER-2 high-altitude airplane, *Nucl. Instr. and Meth. A,* **476**, 42-51, 2002.

Heinrich, W., S. Roesler, and H. Schraube, Physics of cosmic radiation fields, *Radiat. Prot. Dosim.,* **86**, 253-258, 1999.

Hudson, M. K., B. T. Kress, J. E. Mazur, K. L. Perry, and P. L. Slocum, 3D modeling of shock-induced trapping of solar energetic particles in the Earth's magnetosphere, *J. Atmos. Solar-Terr. Phys.,* **66**, 1389, doi:10.1016/j.jastp.2004.04.024, 2004.

Kahler, S. W., Origin and properties of solar energetic particles in space, *in Space Weather, AGU Monograph Series,* vol. 125, edited by P. Song, H. J. Singer, and G. L. Siscoe, American Geophysical Union, Washington DC, 2001.

Kalnay et al., The NCEP/NCAR 40-year reanalysis project, *Bull. Amer. Meteor. Soc.,* **77**, 437-470, 1996.

Kress, B. T., M. K. Hudson, and P. L. Slocum, Impulsive solar energetic ion trapping in the magnetosphere during geomagnetic storms, *Geophys. Res. Lett.*, **32**, L06108, doi:10.1029/2005GL022373, 2005.

Kress, B. T., M. K. Hudson, K. L. Perry, and P. L. Slocum, Dynamic modeling of geomagnetic cutoff for the 23-24 November 2001 solar energetic particle event, *Geophys. Res. Lett.*, **31**, L04808, doi:10.1029/2003GL018599, 2004.

Kuhn, E., F. E. Schwamb, and W. T. Payne, Solar Flare to Earth-Orbiting Vehicles, *Second Symposium on Protection Against Radiations in Space,* NASA SP-71, 429-434, 1965.

Lambiotte, J. J., J. W. Wilson, and T. A. Filipas, PROPER-3C: A Nucleon-Pion Transport Code, *NASA TM X-2158,* 1971.

Langlais, B., and M. Mandea, An IGRF candidate geomagnetic field model for epoch 2000 and a secular variation model for 2000-2005, *Earth Planets Space*, **52**, 1137-1148, 2000.

Luhmann, J. G., S. C. Solomon, J. A. Linker, J. G. Lyon, Z. Mikic, D. Odstrcil, W. Wang, and M. Wiltberger., Coupled model simulation of a Sun-to-Earth space weather event, *J. Atmos. Solar-Terr. Phys.,* **66**, 1243, doi:10.1016/j.jastp.2004.04.005, 2004.

Lyon, J. G., J. A. Fedder, and C. M. Mobarry, The Lyon-Fedder, Mobarry (LFM) global MHD magnetospheric simulation code, *J. Atmos. Solar-Terr. Phys.,* **66**, 1333, doi:10.1016/j.jastp.2004.03.020, 2004.

Mavromichalaki, H., G. Souvatzoglou, G. Mariatos, C. Plainaki, M. Gerontidou, A. Belov, E. Eroshenko, and V. Yanke, Space weather prediction by cosmic rays, *Adv. Space Res.*, **37**, 1141-1147, 2006.

Menn, W., M. Hof, and O. Reimer, et al., The absolute flux of protons and helium at the top of the atmosphere using IMAX, *Astrophysical Journal*, **533**, 281-297, 2000.

Mertens, C. J., J. W. Wilson, S. A. Walker, and J. Tweed, Coupling of multiple Coulomb scattering with energy loss and straggling in HZETRN, *Adv. Space Res.*, **40**, 1357-1367, 2007.

Mewaldt, R. A., C. M. S. Cohen, A. W. Labrador, R. A. Leske, G. M. Mason, M. I. Desai, M. D. Looper, J. E. Mazur, R. S. Selesnick, and D. K. Haggerty, Proton,

helium, and electron spectra during the large solar particle events of October-November 2003, *J. Geophys. Res.,* **110**, A09S18, doi:10.1029/2005JA011038, 2005.
Neher, H. V., Cosmic rays at high latitudes and altitudes covering four solar maxima, *J. Geophys. Res.,* **76**, 1637-1851, 1971.
Neher, H. V., Cosmic-ray particles that changed from 1954 to 1958 to 1965, *J. Geophys. Res.,* **72**, 1527-1539, 1967.
Neher, H. V., and H. R. Anderson, Cosmic rays at balloon altitudes and the solar cycle, *J. Geophys. Res.,* **67**, 1309-1315, 1962.
Neher, H. V., Cosmic-ray knee in 1958, *J. Geophys. Res.,* **66**, 4007-4012, 1961.
Norbury, J. W., Nucleon-nucleon total cross section, submitted as NASA Technical Paper, 2007a.
Norbury, J. W., Pion and kaon lab frame differential cross sections for intermediate energy nucleus-nucleus collisions, submitted as NASA Technical Paper, 2007b
Parker, E. N., The passage of energetic charged particles through interplanetary space, *Planet. Space Sci.,* **13**, 9-49, 1965.
Reitz, G., K. Schnuer, and K. Shaw, Editorial — Workshop on radiation exposure of civil aircrew, *Radiat. Prot. Dosim.,* **48**, 3, 1993.
Shea, M. A., and D. F. Smart, A world grid of calculated cosmic ray vertical cutoff rigidities for 1980.0, *18th International Cosmic Ray Conference-Conference Papers,* MG Session, Vol. 3, Tata Instr. of Fundmental Research (Colaba, Bombay), 415-418, 1983.
Smart, D. F., and M. A. Shea, A comparison of the Tsyganeko model predicted and measured cutoff latitudes, *Adv. Space Res.*, **28**, 1733-1738, 2001.
Smart D. F., M. A. Shea, and E. O. Fluckiger, Magnetospheric models and trajectory computations, *Space Science Reviews*, **93**, 305-333, 2000.
Spence, H., D. Baker, A. Burns, T. Guild, C.-L., Huang, G. Siscoe, and R. Weigel, Center for integrated space weather modeling metrics plan and initial model validation results, *J. Atmos. Solar-Terr. Phys.,* **66***,* 1499, doi:10.1016/j.jastp.2004.03.029, 2004.
Tsyganenko, N. A. and M. I. Sitnov, Modeling the dynamics of the inner magnetosphere during strong geomagnetic storms, *J. Geophys. Res.,* **110**, A03208, doi:10.1029/2004JA010798, 2005.
Tsyganenko, N., A model of the near magnetosphere with dawn-dusk asymmetry: 1. Mathematical structure, *J. Geophys. Res.*, **107(A8)**, 1179, doi:10.1029/2001JA000219, 2002.
Tsyganenko, N., Determination of magnetospheric current system parameters and development of experimental geomagnetic field models based on data from IMP and HEOS satellite, *Planet Space Sci*., **37**, 5-20, 1989.
Wallance, R. G., and C. A. Sondhaus, Cosmic ray exposure in subsonic air transport, *Aviation Space, and Environ. Med.,* **74**, 6494-6496, 1978.
Wang, W., T. L. Kileen, A. G. Burns, R. G. Roble, A high resolution, three-dimensional, time dependent, nested grid model of the coupled thermosphere-ionosphere, *J. Atmos. Solar. Terr. Phys.*, **61**, 385-397, 1999.
Weygand, J. M., and J. Raeder, Cosmic ray cutoff prediction using magnetic field from global magnetosphere MHD simulations, *Annales Geophysicae*, **23**, 1441-1453, 2005.

Wilson, J. W., C. J. Mertens, P. Goldhagan, W. Friedberg, G. De Angelis, J. M. Clem, K. Copeland, and H. B. Bidasaria, Atmospheric ionizing radiation and human exposure, *NASA/TP-2005-213935*, 2005.

Wilson, J. W., R. K. Tripathi, C. J. Mertens, S. R. Blattnig, M. S. Clowdsley, F. A. Cucinotta, J. Tweed, J. H. Heinbockel, S. A. Walker, and J. E. Nealy, Verification and ValidationL High Charge and Energy (HZE) Transport Codes and Future Development, *NASA/TP-2005-000000*, 2005b.

Wilson, J. W., J. Tweed, S. A. Walker, F. A. Cucinotta, R. K. Tripathi, S. Blattnig, and C. J. Mertens, A benchmark for laboratory exposures with 1 A GeV iron ions, *Adv. Space Res.,* **35***,* 185-193*,* 2004.

Wilson, J. W., I. W. Jones, D. L. Maiden, and P. Goldhagan (Eds.), Proceedings of the workshop on Atmospheric Ionizing Radiation (AIR): Analysis, results, and lessons learned from the June 1997 ER-2 campaign, *NASA CP-2003-212155*, NASA Langley Research Center, Hampton, Virginia, 2003a.

Wilson, J. W., J. E. Nealy, and G. De Angelis, F. F. Badavi, C. P. Hugger, F. A. Cucinotta, and M. Y. Kim, Dynamic/Anisotropic Low Earth Orbit Environmental Models, Proc. *AIAA 2003-6621*, 23-25 September, Long Beach, California, 2003b.

Wilson, J. W., Overview of radiation environments and human exposures, *Heath Phys.,* **79(5)**, 2000.

Wilson, J. W., *Shielding Strategies for Human Space Exploration,* NASA Conference Publications 3350, edited by J. W. Wilson, J. Miller, A. Konradi, and F. A. Cucinotta, 1997.

Wilson, J. W., L. W. Townsend, W. Schimmerling, G. S. Khandelwal, F. Khan, J. E. Nealy, F. A. Cucinotta, L. C. Simonsen, J. L. Shinn, and J. W. Norbury, Transport Methods and Interactions for Space Radiations, *NASA RP-1257,* 1991.

Wilson, J. W., and L. W. Townsend, Radiation safety in commercial air traffic: A need for further study, *Health Phys.,* **55**, 1001-1003, 1988.

Wilson, J. W., L. W. Townsend, and B. B. Badavi, Galactic HZE propagation through the Earth's atmosphere, *Radiat. Res.,* **109**, 173-183, 1987.

Wilson, J. W., and F. F. Badavi, Methods of galactic heavy-ion transport, *Radiat. Res.,* 231, 1986.

Wilson, J. W., J. J. Lambiotte, T. Foelsche, and T. A. Filippas, Dose Response Functions in the Atmosphere Due to Incident High-Energy Protons with Applications to Solar Proton Events*, NASA TN D-6010,* 1970.

Wiltberger, M., W. Wang, A. G. Burns, S. C. Solomon, J. G. Lyon, and C. C. Goodrich, Initial results from the coupled magnetosphere-ionosphere-thermosphere model: magnetospheric and ionospheric responses, *J. Atmos. Solar-Terr. Phys.*, **66**, 1411, doi:10.1016/j.jastp.2004.04.026, 2004.

Table 1: Linear fit coefficients between the GCR model solar modulation parameter and the Climax neutron monitor count rate for the three states of solar magnetic field polarity

Solar Modulation Parameter = A + B*Climax		
Solar Magnetic Field Polarity	**A**	**B**
Positive	5434.50	-1.15674
Negative	4534.20	-0.92760
Transition	8253.75	-1.88870

Table 2: GOES/SEM EPS and HEPAD channels used to derive proton and alpha fluence spectra

Particle	Channel Designation	Energy Range (MeV)	Instrument
Proton	P2	4-9	EPS (differential)
Proton	P3	9-15	EPS (differential)
Proton	P4	15-40	EPS (differential)
Proton	P5	40-80	EPS (differential)
Proton	P6	80-165	EPS (differential)
Proton	P7	165-500	EPS (differential)
Proton	P8	350-420	HEPAD
Proton	P9	420-510	HEPAD
Proton	P10	510-700	HEPAD
Proton	I3-I2	5-10	EPS (>10 - >5)
Proton	I4-I3	10-30	EPS (>30 - >10)
Proton	I5-I4	30-50	EPS (>50 - >30)
Proton	I6-I5	50-60	EPS (>60 -> 50)
Proton	I7-I6	60-100	EPS (>100 - >60)
Alpha	A1	4-10	EPS (differential)
Alpha	A2	10-21	EPS (differential)
Alpha	A3	21-60	EPS (differential)
Alpha	A4	60-150	EPS (differential)
Alpha	A5	150-250	EPS (differential)
Alpha	A7	2560-3400	HEPAD

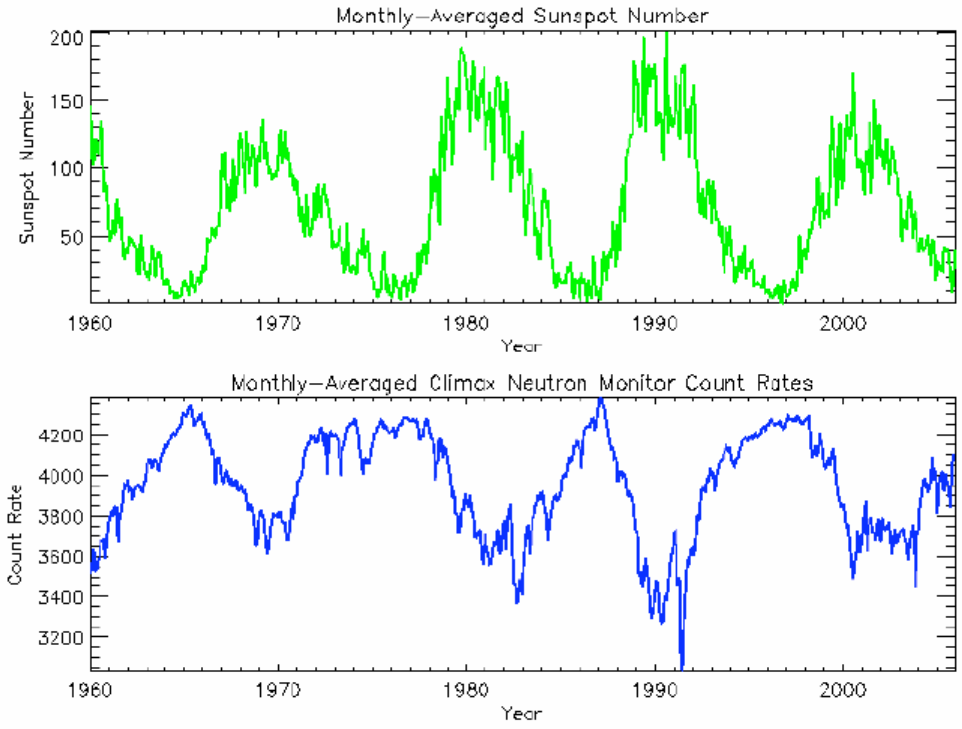

Figure 1: Illustration of anti-correlation between solar cycle modulation and local incident GCR flux. – as indicated by the neutron counts. The top panel shows monthly-averaged sun spot number from 1960-2005. The bottom panel shows monthly-averaged neutron monitor count rates from the Climate site.

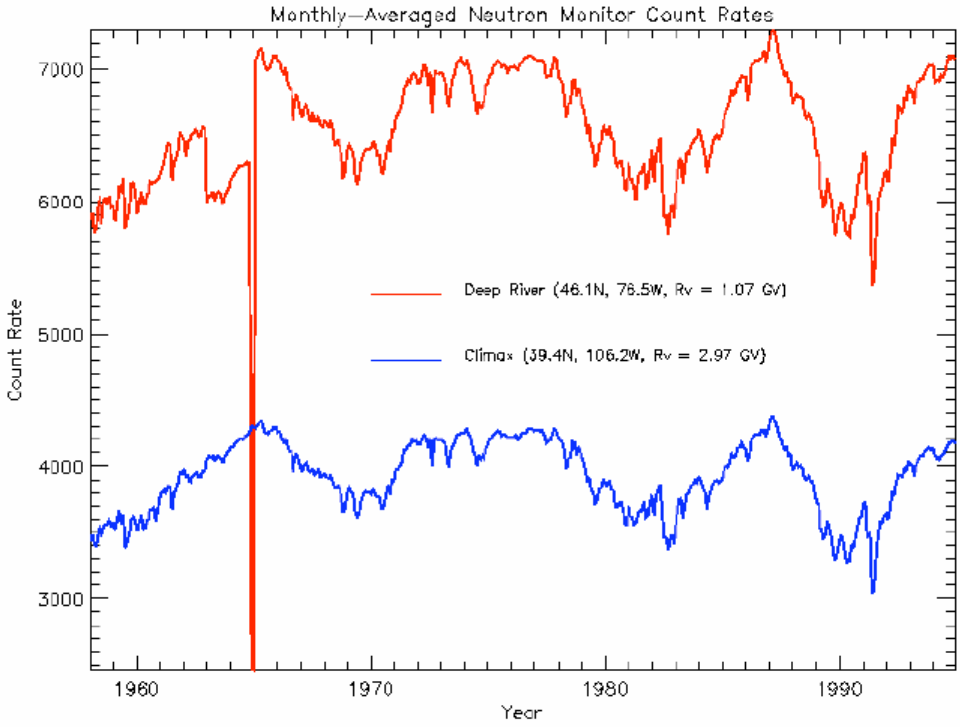

Figure 2: Neutron count rates measured from the Deep River site (red line) and the Climax site (blue line) from 1958-1995. The Deep River count rates are suspect from 1963-1964 and indicate an instrument problem.

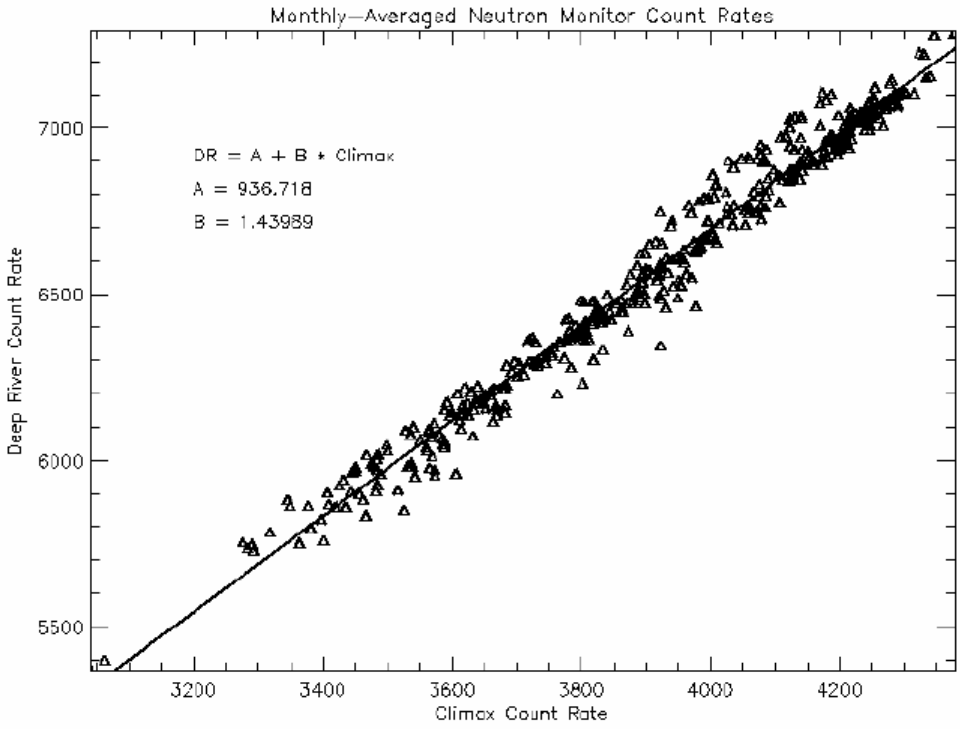

Figure 3: Linear fit between Deep River neutron monitor count rates and Climax monitor count rates. DR in the legend refers to neutron count rates at the Deep River site.

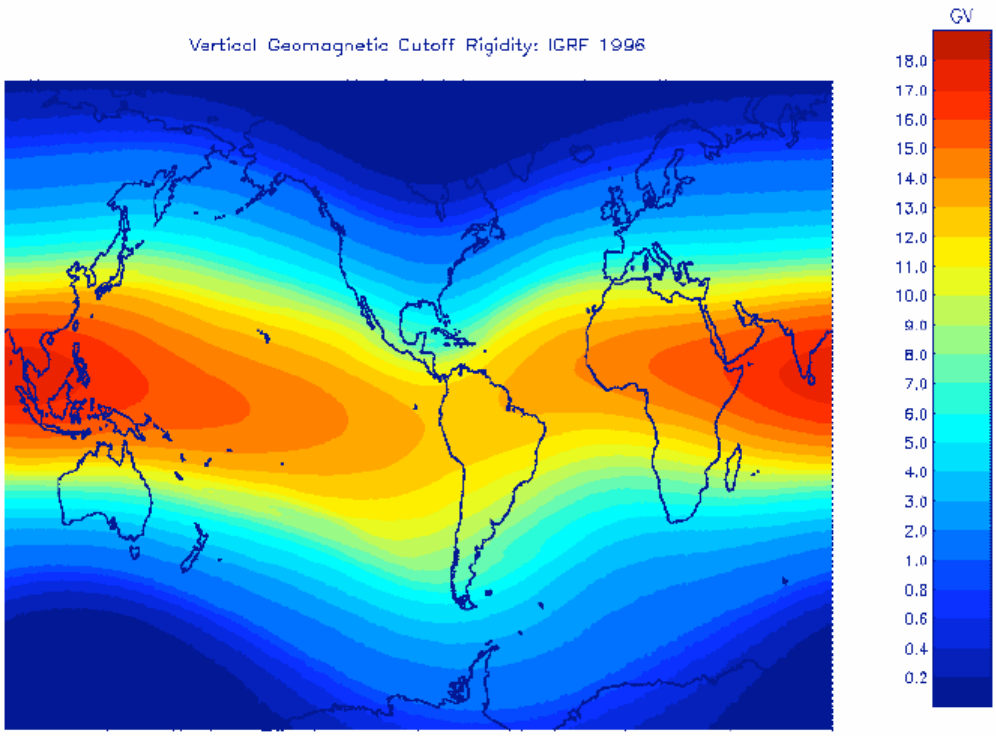

Figure 4: Global grid of quiescent vertical geomagnetic cutoff rigidities (GV) calculated from charged particle trajectory simulations using the IGRF model for the 1996 epoch (solar cycle 23 minimum).

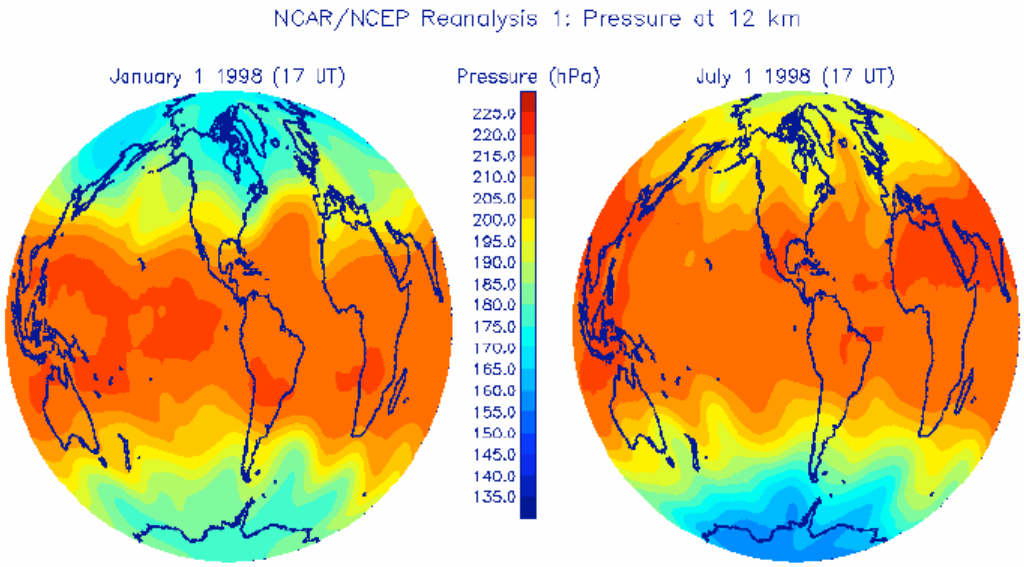

Figure 5: Global distribution of atmospheric pressure (hPa) at 12 km obtained from the NCAR/NCEP Reanalysis 1 geopotential height product. The left panel shows the pressure data on January 1, 1998 at 17 UT. The right panel shows the pressure data on July 1, 1998 at 17 UT.

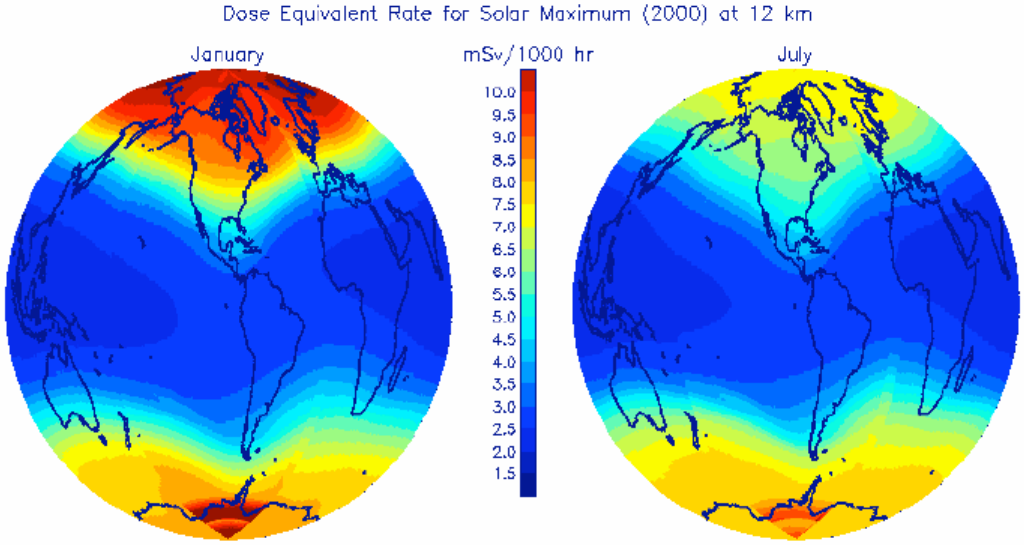

Figure 6: Global distribution of dose equivalent rate (mSv/1000 hr) predicted by the parametric AIR model at 12 km for solar maximum conditions (year 2000) of cycle 23.

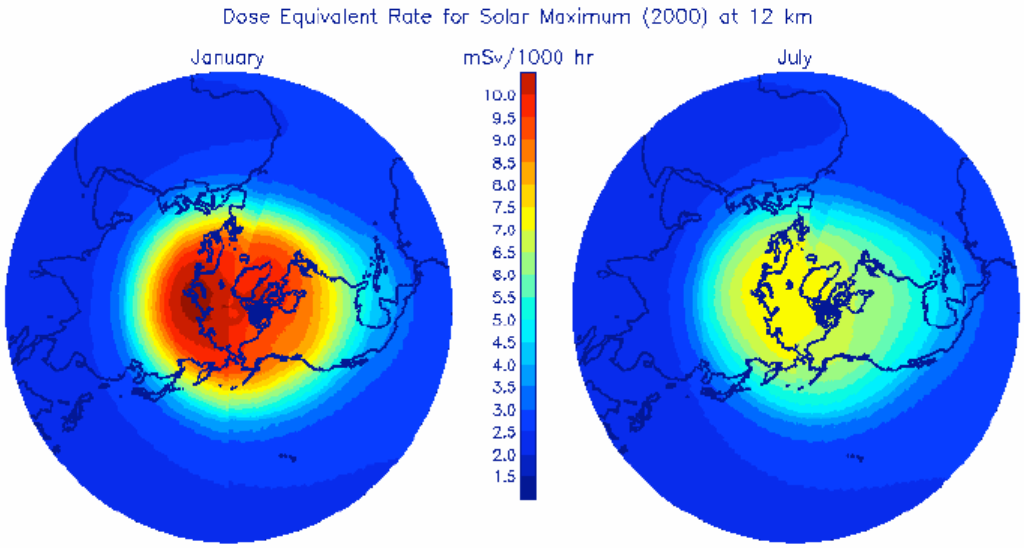

Figure 7: Northern hemisphere polar view of Figure 6.

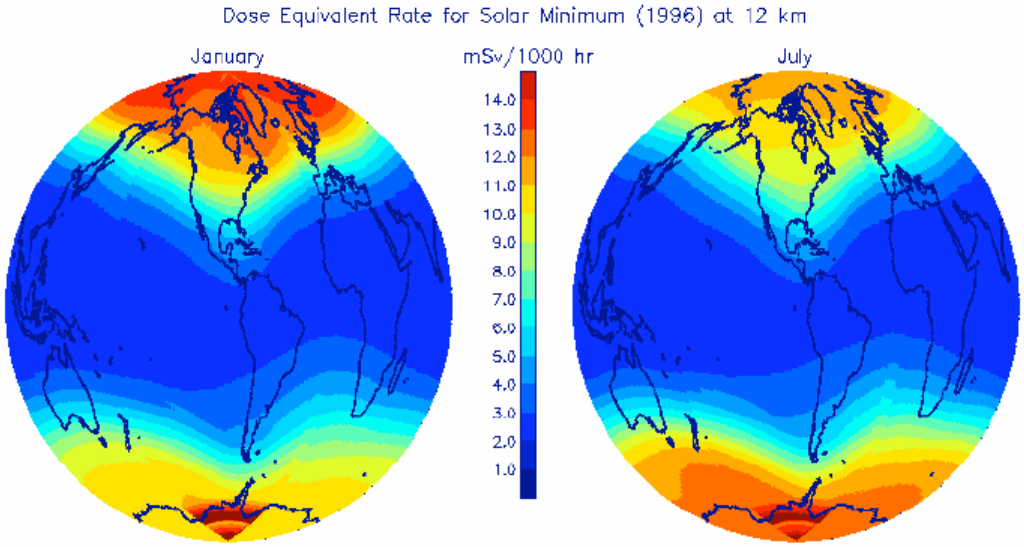

Figure 8: Global distribution of dose equivalent rate (mSv/1000 hr) predicted by the parametric AIR model at 12 km for solar minimum conditions (year 1996) of cycle 23.

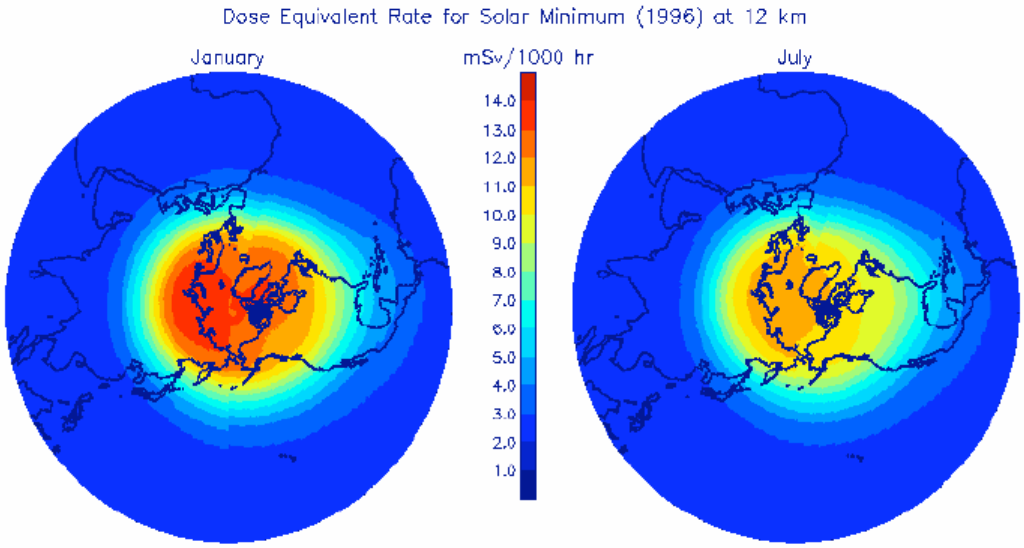

Figure 9: Northern hemisphere polar view of Figure 8.

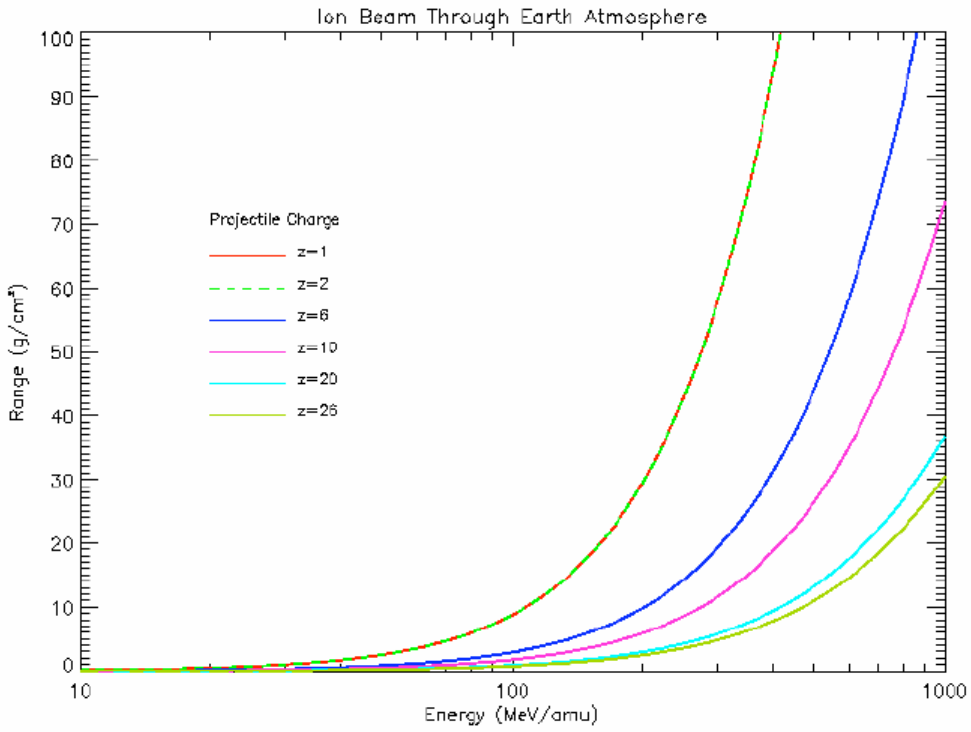

Figure 10: Range-energy relations for ion beam transport through the atmosphere. The charge number (z) of the ion is specified in the legend.

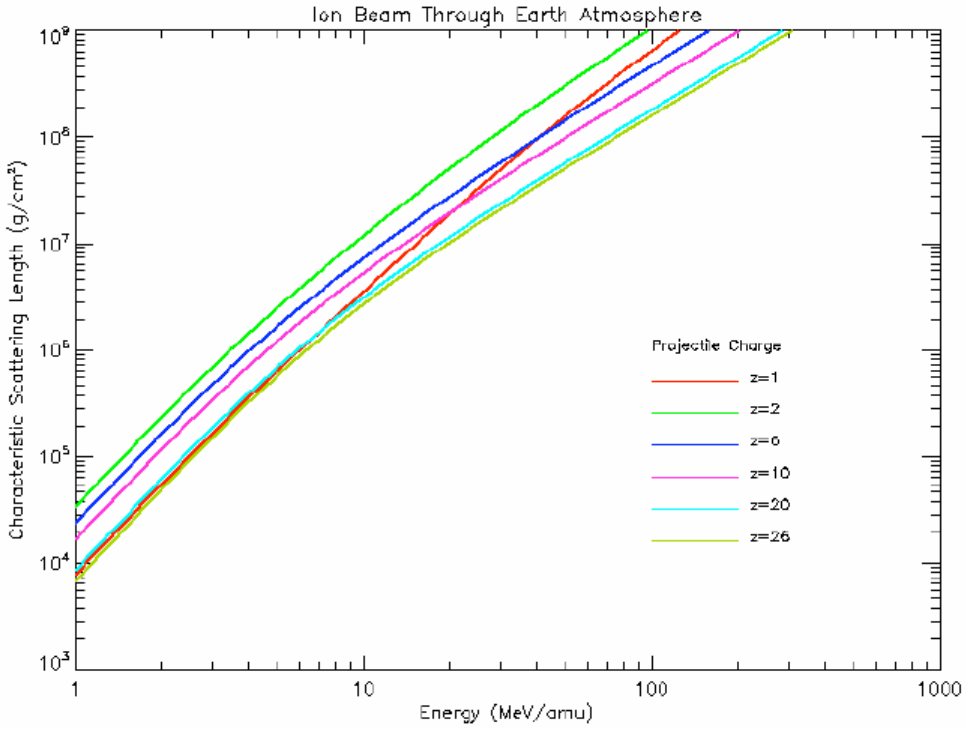

Figure 11: Characteristic scattering length for ion beam transport through the atmosphere. The charge number (z) of the ion is specified in the legend.

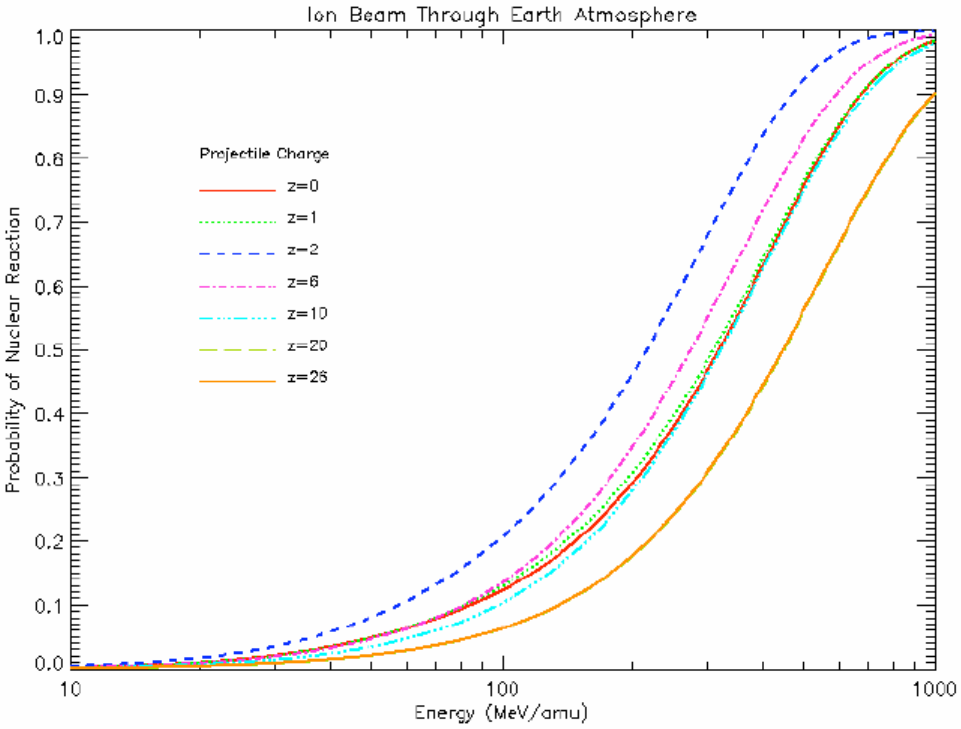

Figure 12: Probability of nuclear reaction for ion beam transport through the atmosphere. The charge number (z) of the ion is specified in the legend.

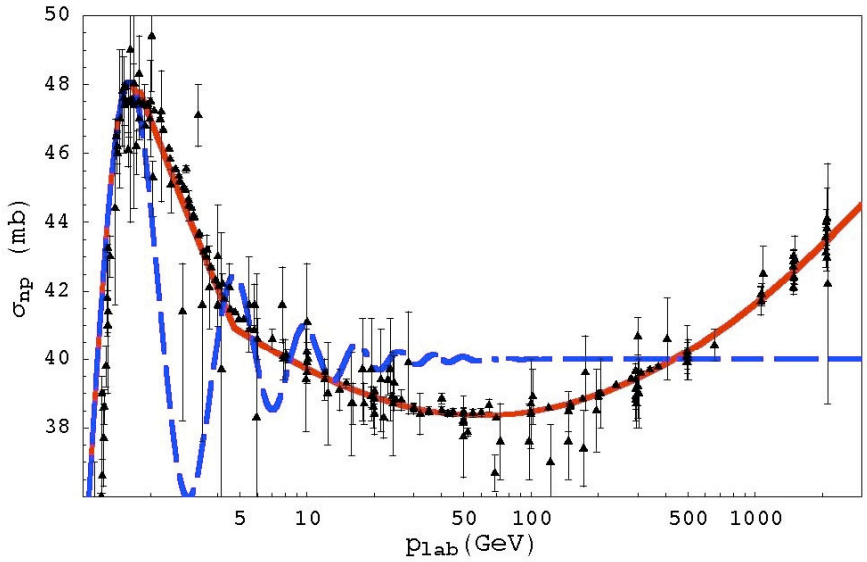

Figure 2: Total proton-proton cross section. The blue dashed curve is used in HZETRN [4] and the red solid curve is the present work. Experimental data are from Reference [6].

Figure 13: See caption embedded in this Figure, which corresponds to Figure 2 from Norbury [2007a].

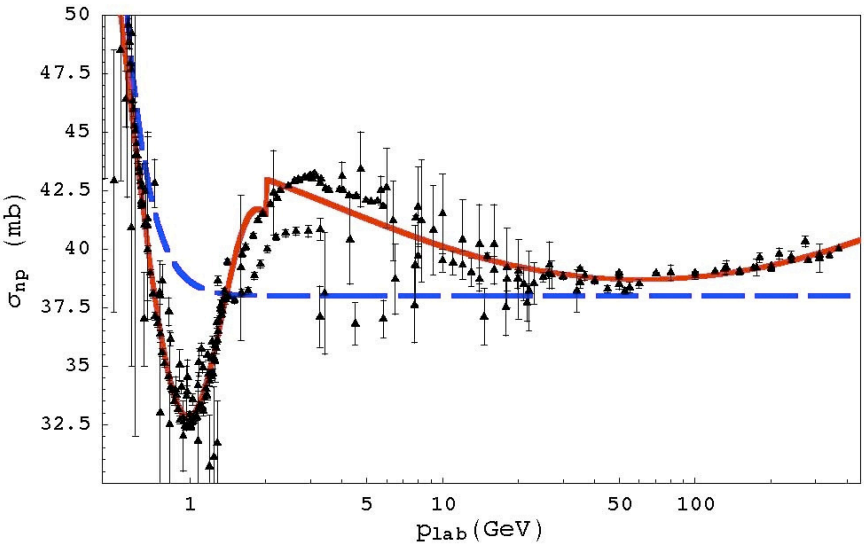

Figure 4: Total proton-neutron cross section. The blue dashed curve is used in HZETRN [4] and the red solid curve is the present work. Experimental data are from Reference [6].

Figure 14: See caption embedded in this figure, which corresponds to Figure 4 from Norbury [2007a].

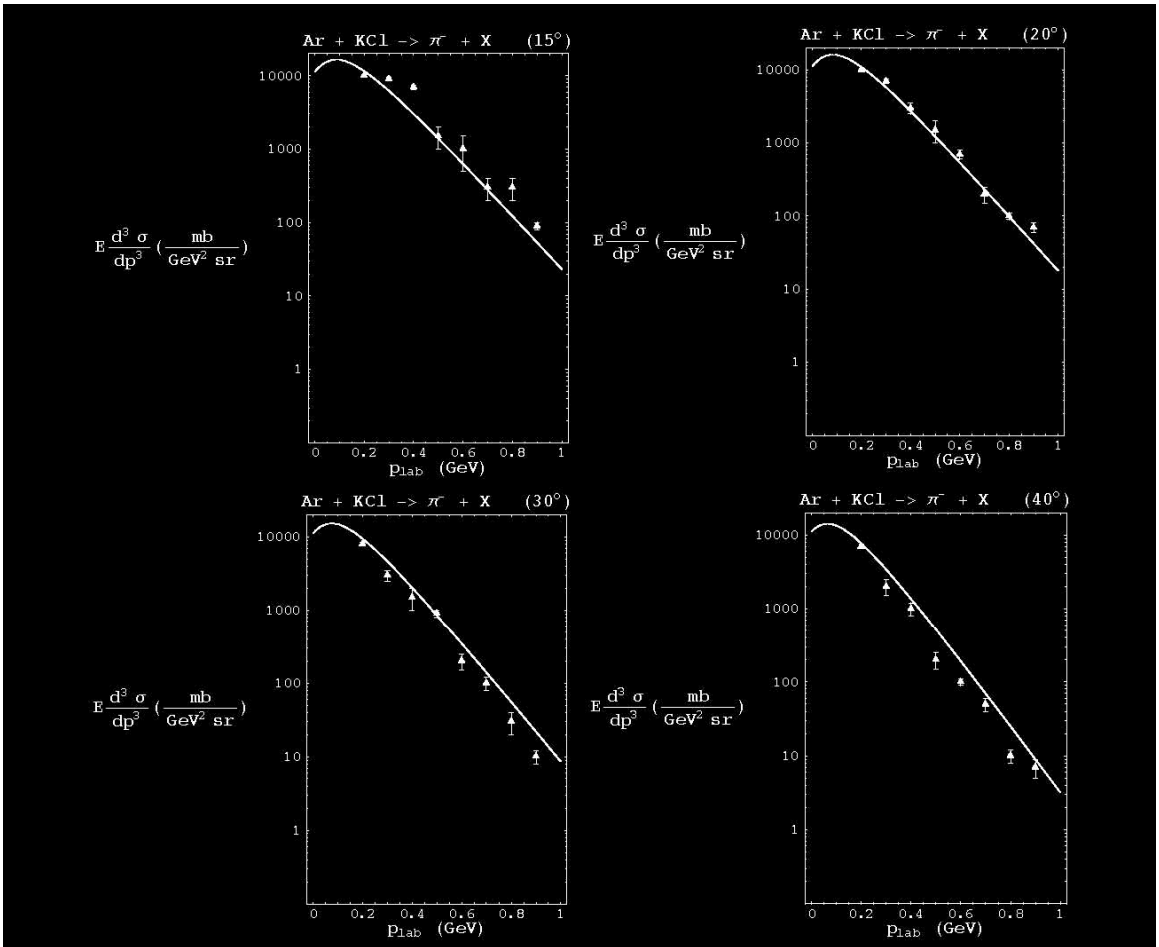

Figure 5: Thermal spectrum successfully describes data at 800 AMeV. The overall normalization from equation (31) was fitted as $N = 1.5 \times 10^5$ mb/GeV^{2}sr. The effective nuclear temperature, taken from reference [30], is $E_0 = 66$ MeV. Lab angles are indicated.

Figure 15: See caption embedded in this figure, which corresponds to Figure 5 from Norbury and Blattnig [2007b].

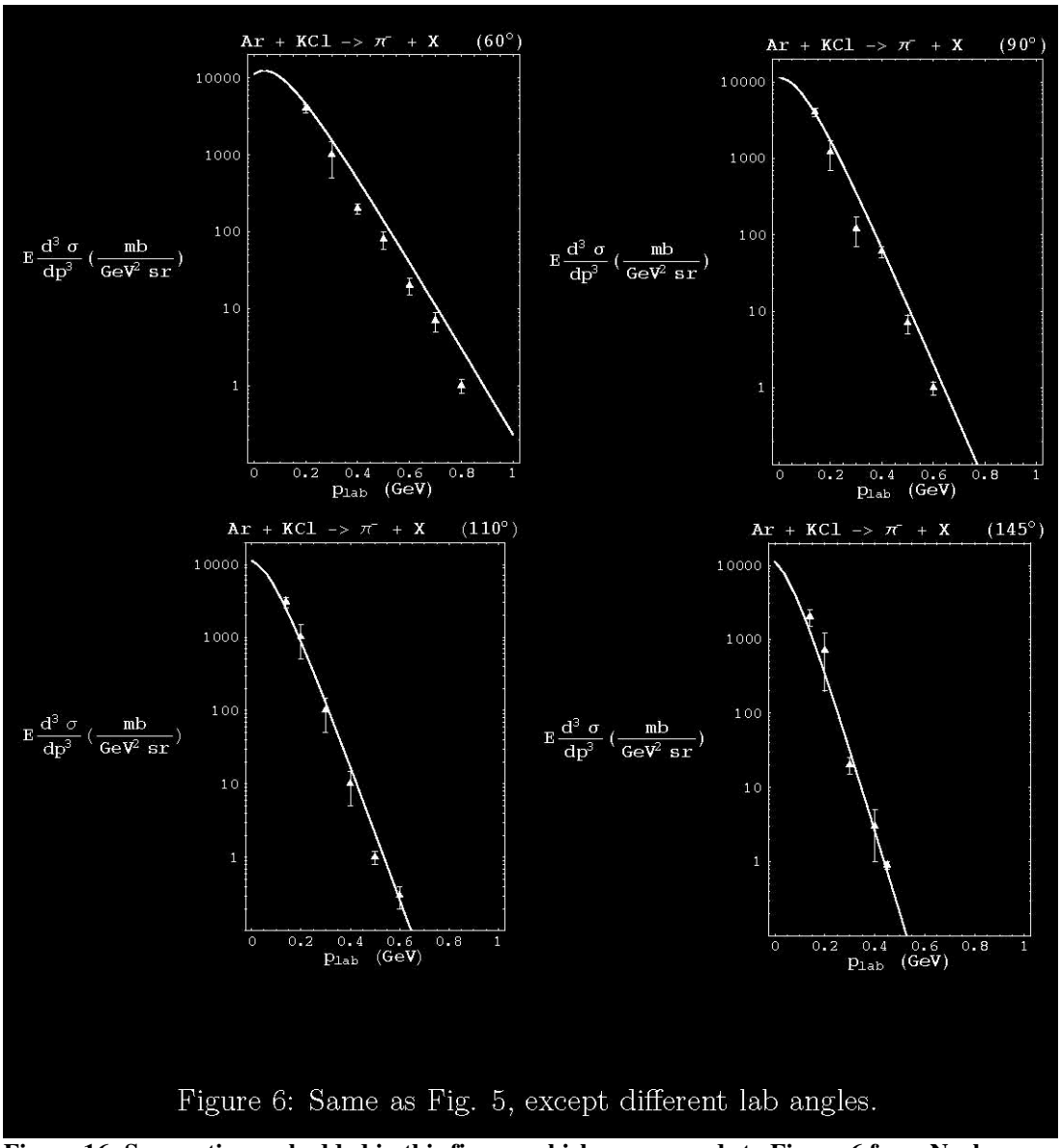

Figure 16: See caption embedded in this figure, which corresponds to Figure 6 from Norbury and Blattnig [2007b].

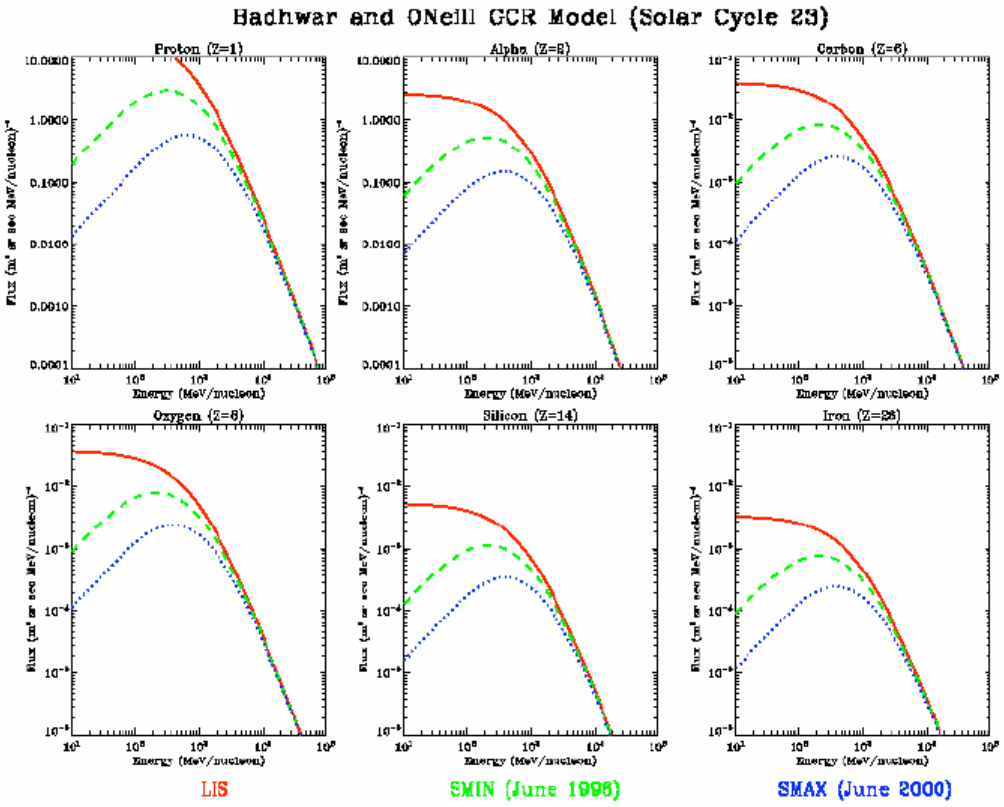

Figure 17: GCR spectral flux for various nuclei predicted by the Badhwar and O'Neill model for solar cycle 23. The local interstellar spectrum (LIS) is denoted by the red lines. Solar minimum spectra are represented by June 1996 conditions, and are denoted by green lines. Solar maximum spectra are represented by June 2000 conditions, and are denoted by blue lines.

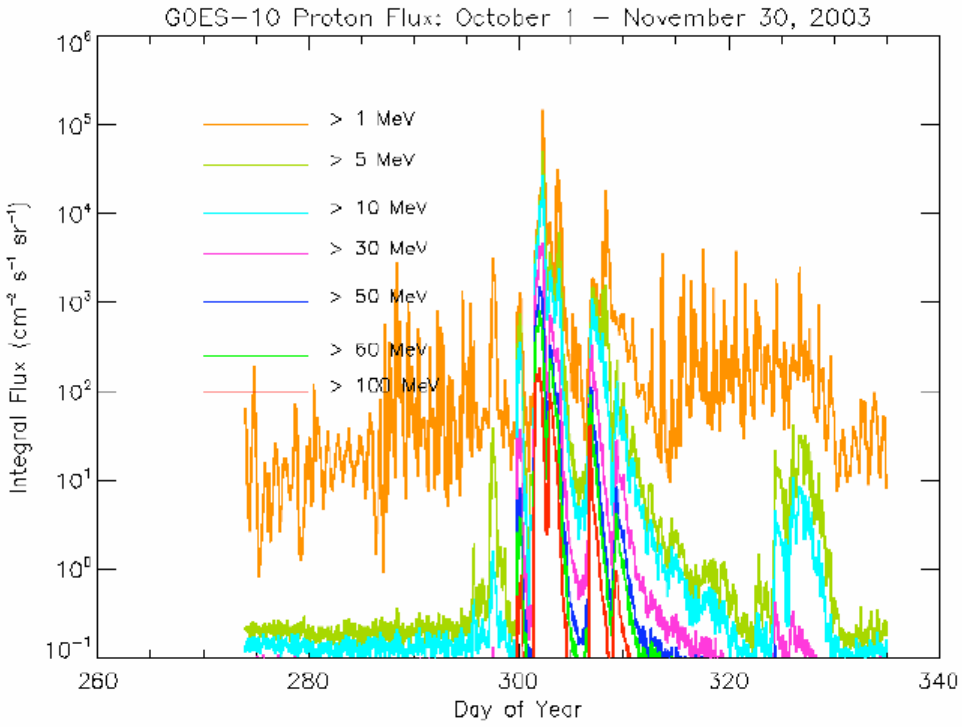

Figure 18: GOES-10 integral proton flux measurements during the Halloween 2003 superstorm event.

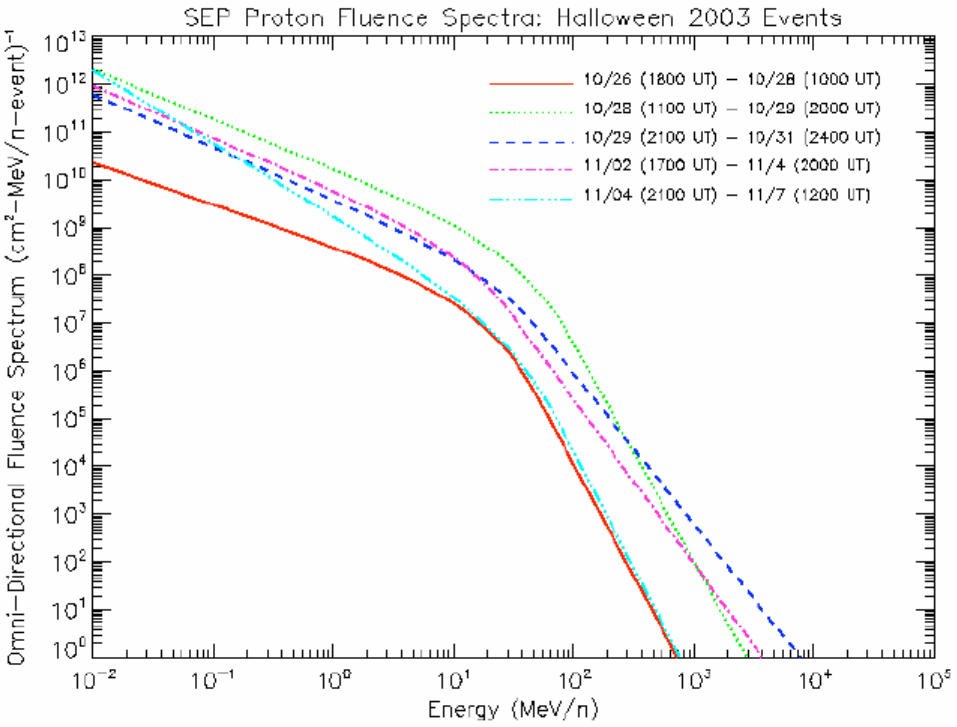

Figure 19: Proton fluence spectra for five SEP events during the Halloween (October-November) 2003 superstorm event.

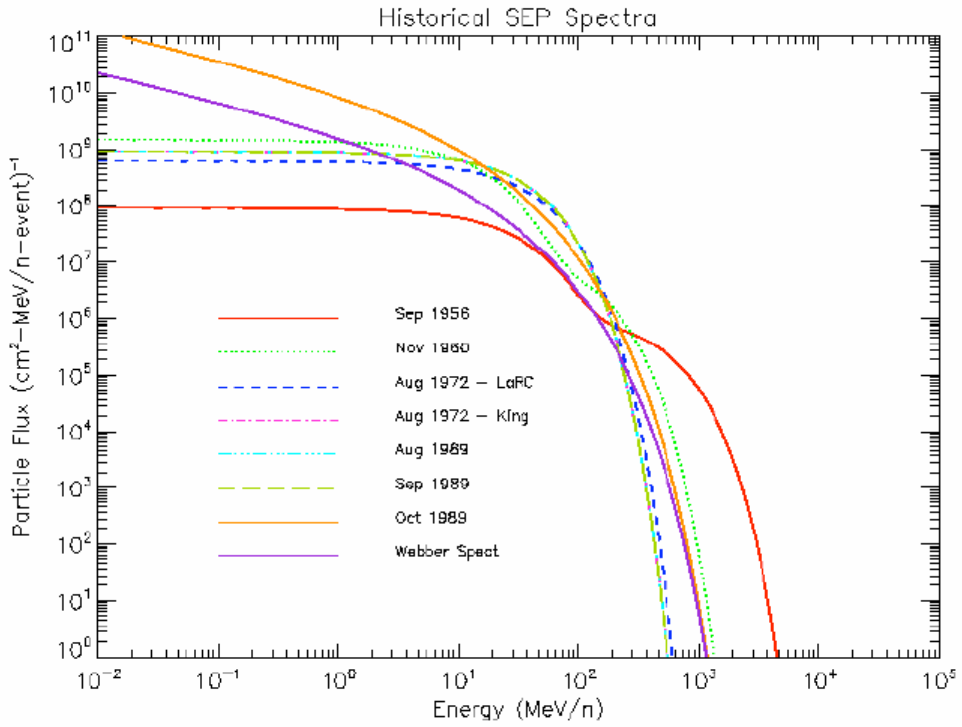

Figure 20: Historical SEP proton fluence spectra used in space radiation engineering design and health risk applications.

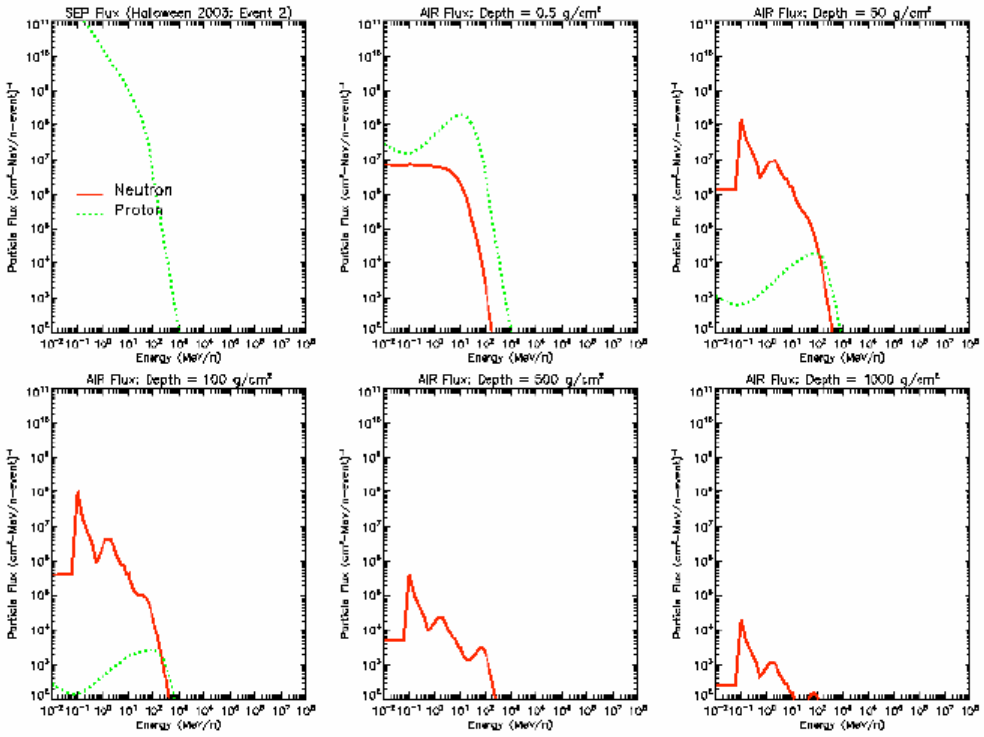

Figure 21: Atmospheric transport of SEP primary and secondary particle spectra computed by HZETRN for zero geomagnetic cutoff rigidity. The top left panel is the incident SEP proton spectrum for event 2 (10/28 (1100 UT) – 10/29 (2000 UT) of the Halloween 2003 storm shown in Figure 19. The remaining panels show the proton and neutron spectrum at various atmospheric depths.

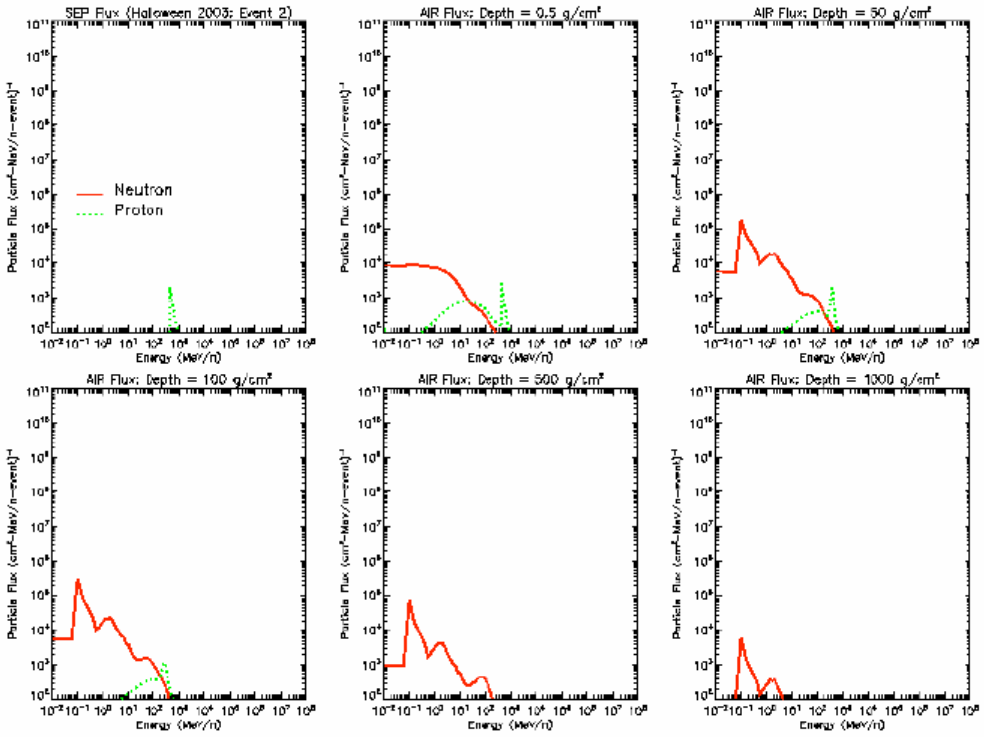

Figure 22: Atmospheric transport of SEP primary and secondary particle spectra computed by HZETRN for 1 GV geomagnetic cutoff rigidity. The top left panel is the incident SEP proton spectrum for event 2 (10/28 (1100 UT) – 10/29 (2000 UT) of the Halloween 2003 storm shown in Figure 19. The remaining panels show the proton and neutron spectrum at various atmospheric depths.

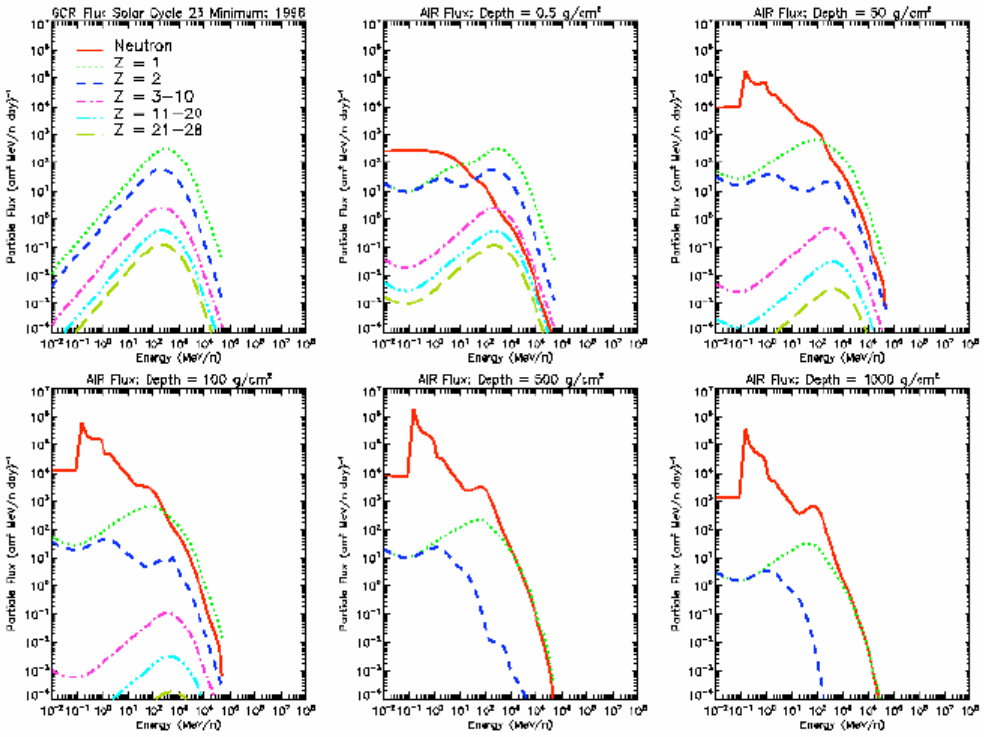

Figure 23: Atmospheric transport of GCR primary and secondary particle spectra computed by HZETRN for zero geomagnetic cutoff rigidity. The top left panel is the 1996 yearly-averaged incident GCR spectrum for solar cycle 23 minimum conditions. The particle flux for various charges have been summed together to reduce the number of line curves. The remaining panels show the GCR spectra at various atmospheric depths.

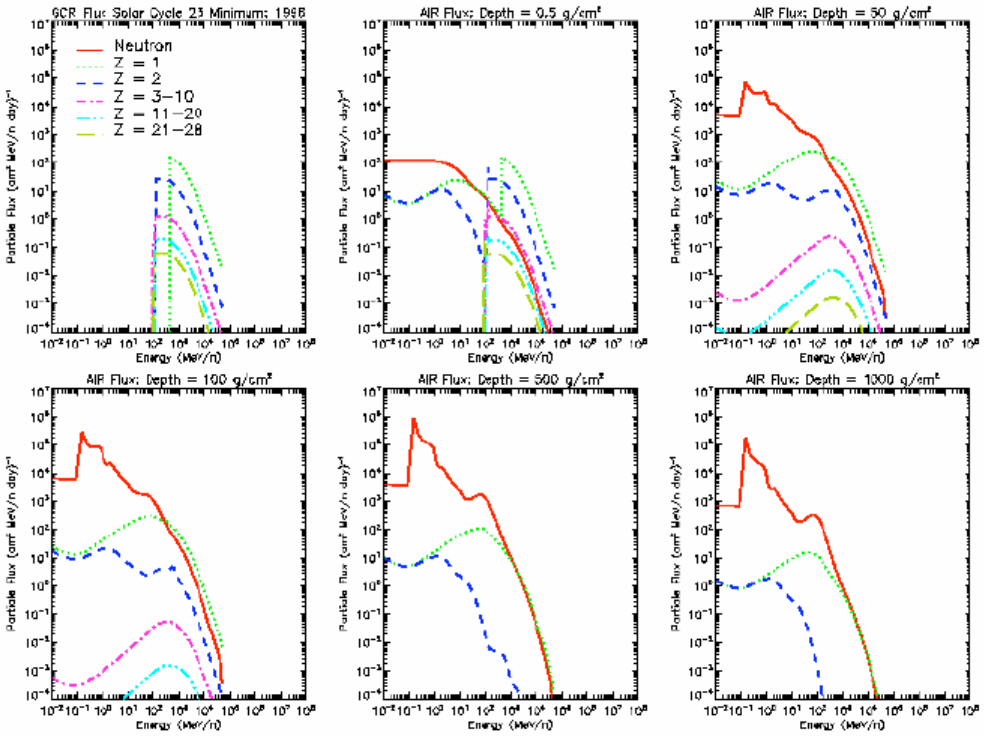

Figure 24: Atmospheric transport of GCR primary and secondary particle spectra computed by HZETRN for 1 GV geomagnetic cutoff rigidity. The top left panel is the 1996 yearly-averaged incident GCR spectrum for solar cycle 23 minimum conditions. The particle flux for various charges have been summed together to reduce the number of line curves. The remaining panels show the GCR spectra at various atmospheric depths.

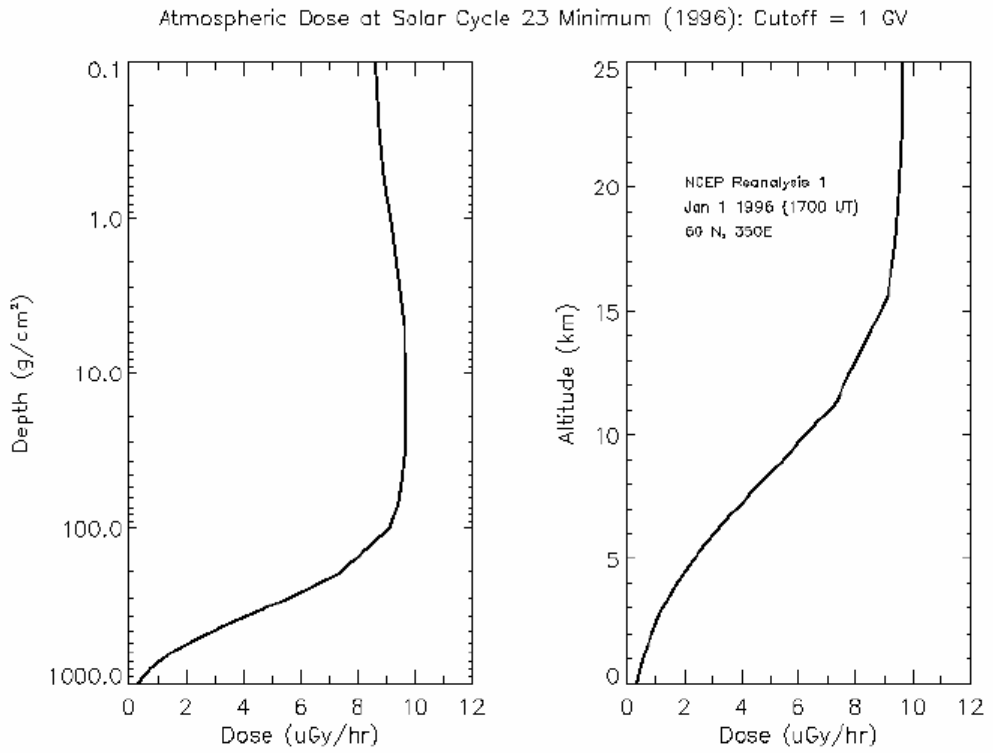

Figure 25: Atmospheric dose (uGy/hr) computed for yearly-averaged incident GCR spectra in 1996, corresponding to solar minimum conditions for cycle 23. The geomagnetic cutoff rigidity was taken to be 1 GV. The left panel shows dose as a function of atmospheric depth (g/cm^2). The right panel shows the dose profile mapped from atmospheric depth to altitude (km) using NCEP Reanalysis 1 geopotential height data at 60N, 350E on January 1, 1996 at 17:00 UT.

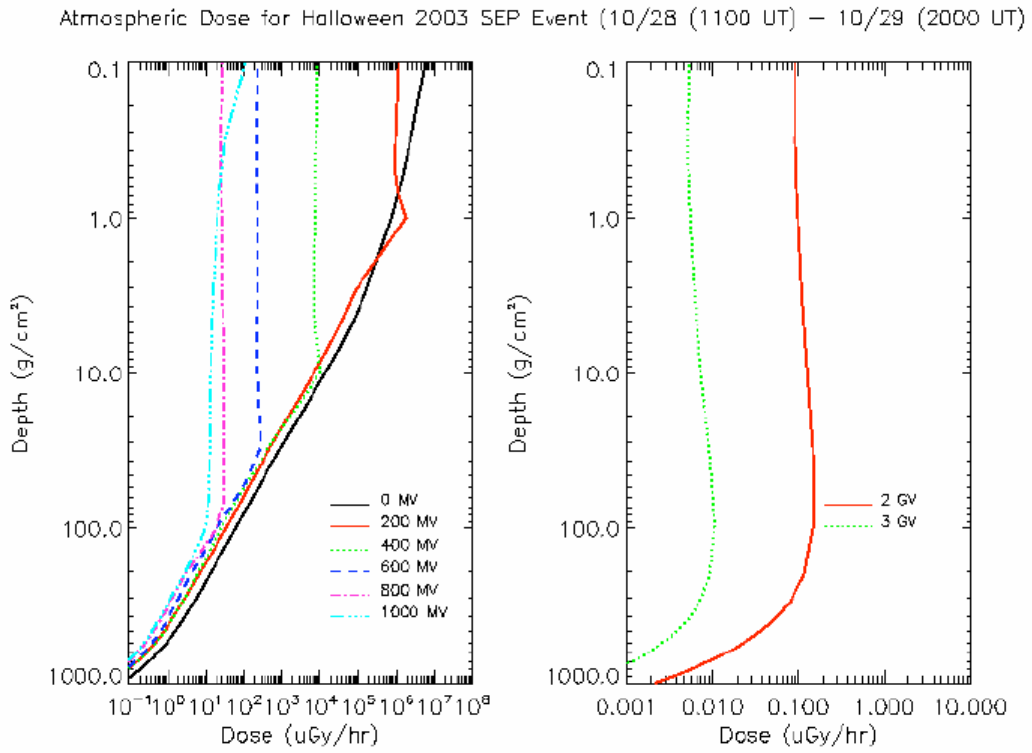

Figure 26: Air dose rates as a function of atmospheric depth for a SEP event (10/28 (11:00 UT) – 10/29 (20:00 UT)) during the Halloween 2003 superstorm event. The left panel shows the atmospheric dose rates for various geomagnetic cutoff rigidities from zero (polar region) to 1 GV. The right panel shows does rates for 2 and 3 GV cutoffs.

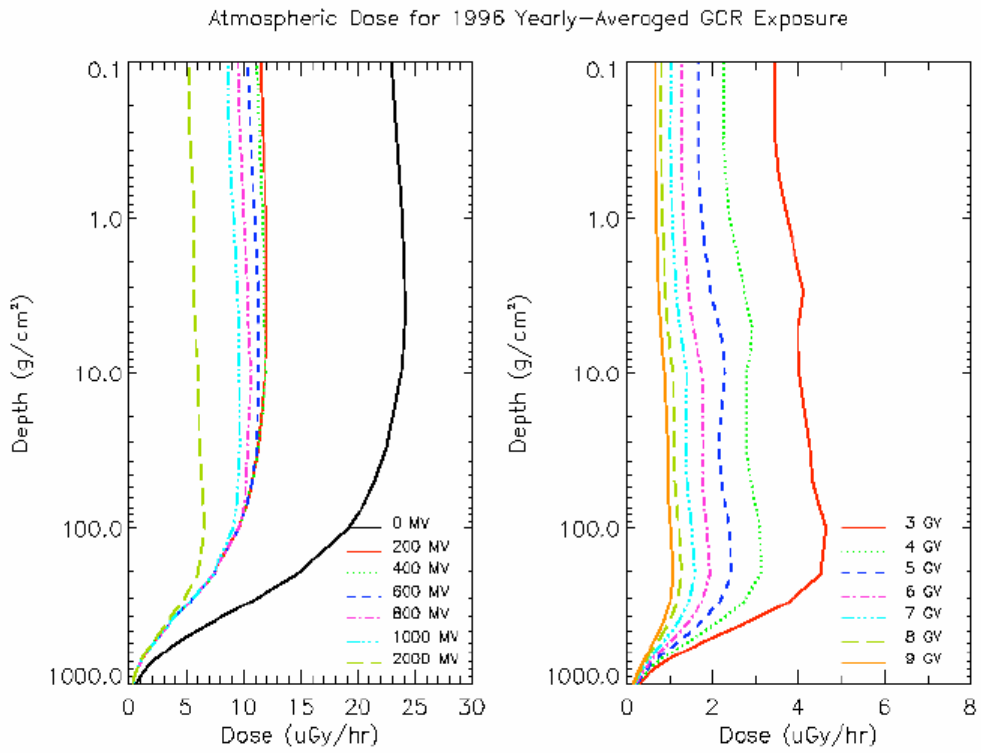

Figure 27: Air dose rates as a function of atmospheric depth for yearly-averaged GCR exposure during solar minimum conditions of cycle 23 (1996). The left panel shows the atmospheric dose rates for various geomagnetic cutoff rigidities from zero (polar region) to 2 GV. The right panel shows does rates for 3-9 GV.

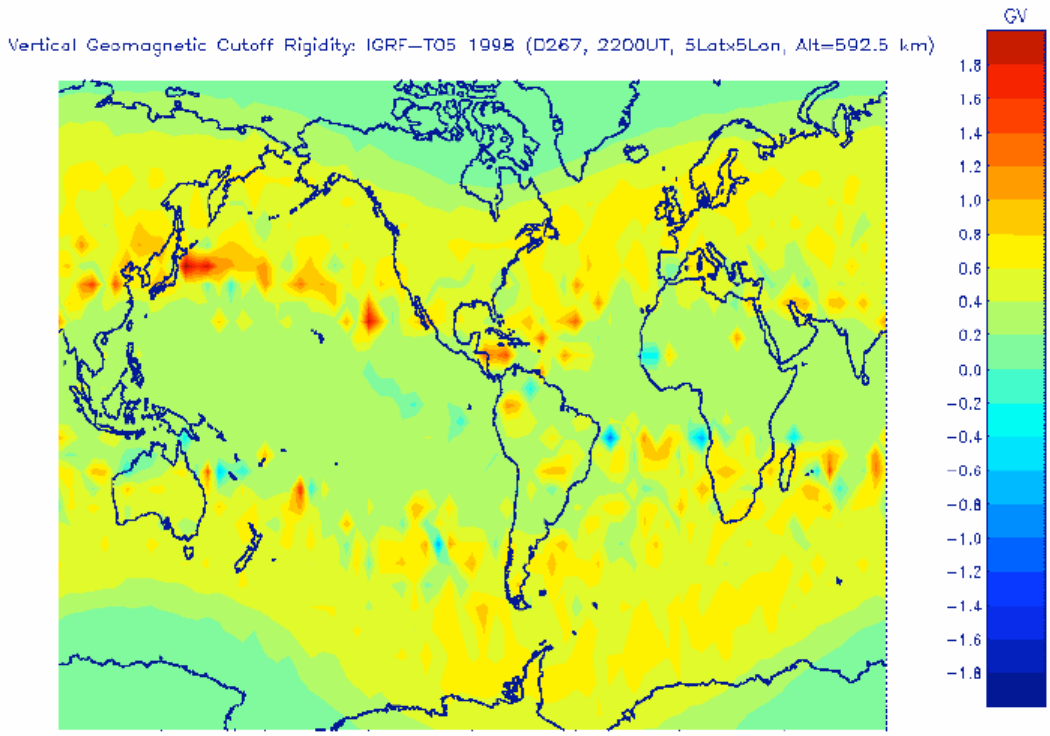

Figure 28: Vertical geomagnetic cutoff rigidity difference (GV) at 22:00 UT on September 24, 1998 using different magnetic field models: IGRF-T05

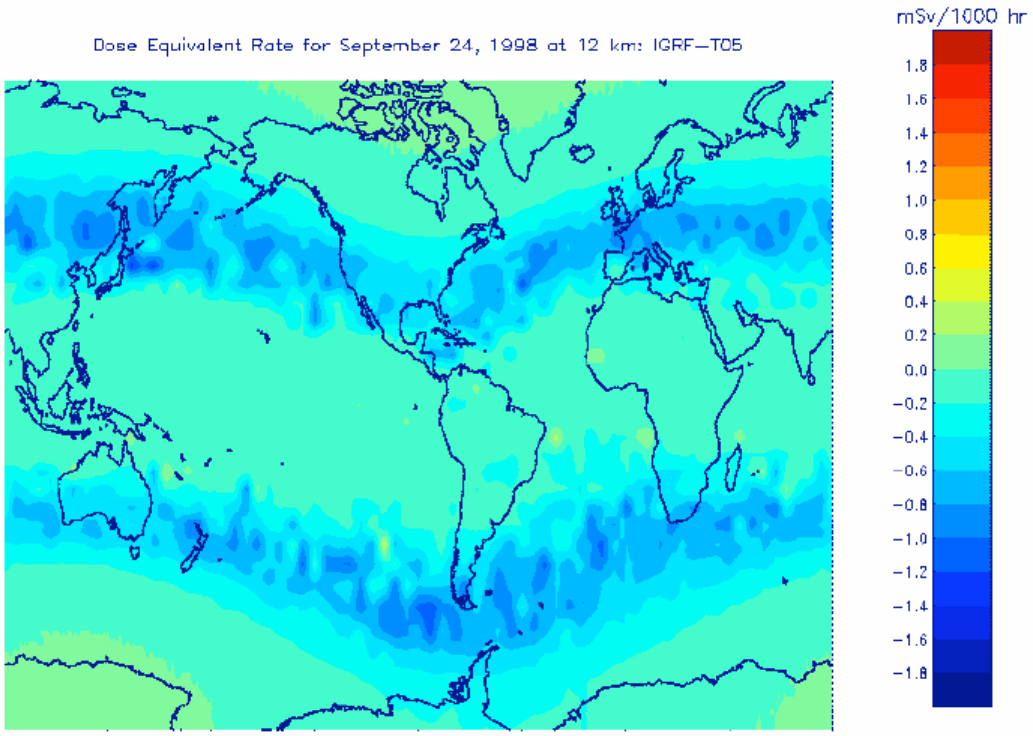

Figure 29: Difference in dose equivalent rate (mSv/1000 hr) at 12 km as a result of using the different magnetic field models in the calculation of vertical geomagnetic cutoff rigidity (i.e., IGRF-T05; see previous Figure).

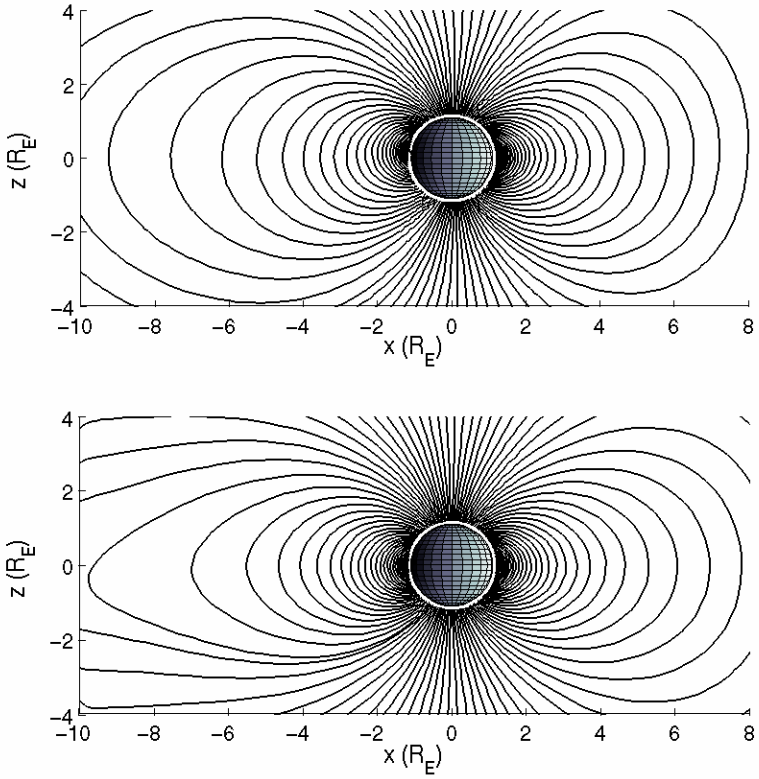

Figure 30: Magnetic field lines in the merdional (x-z) plane in solar magnetospheric coordinates. The sun is directed along the positive x-axis. The magnetic dipole moment is directed along the z-axis. The top panel shows field line computed by the coupled MHD model. The bottom panel shows field lines computed by the T05 model. See section 2.2 for description of the magnetospheric models.

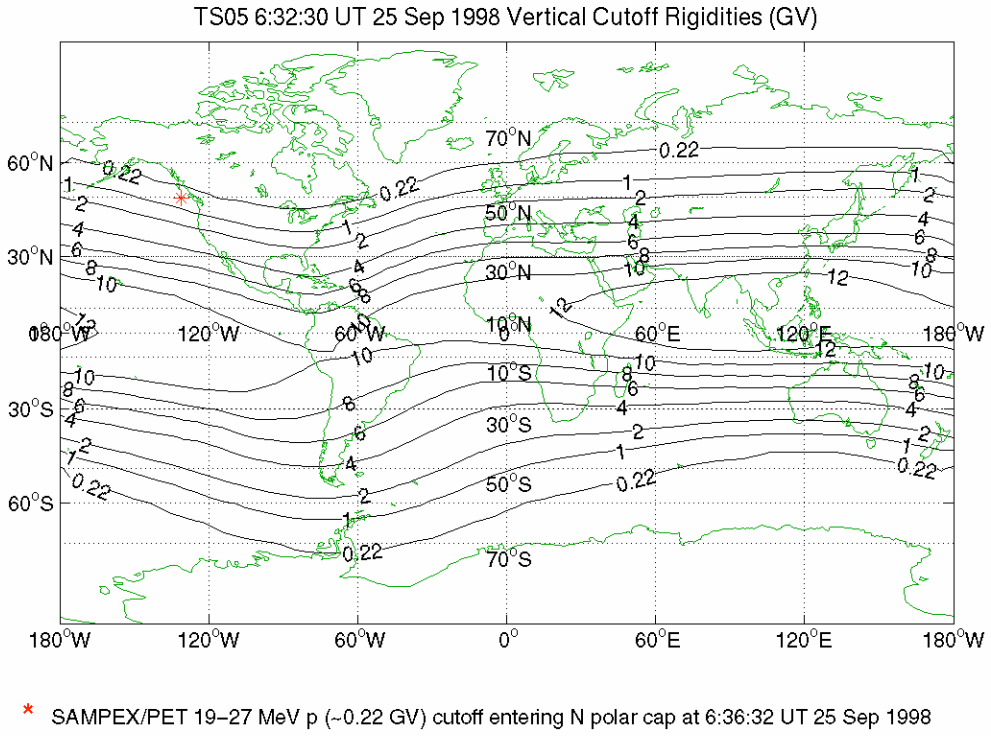

Figure 31: Geomagnetic cutoff rigidities (GV) computed using the T05 magnetospheric magnetic field model for the snap shot at 06:32 UT on September 25, 1998. This snap shot corresponds to the peak solar wind dynamic pressure and minimum Dst-index during this storm period. The SAMPEX observation of cutoff rigidity is shown for the closest time coincidence to the simulated snap shot.

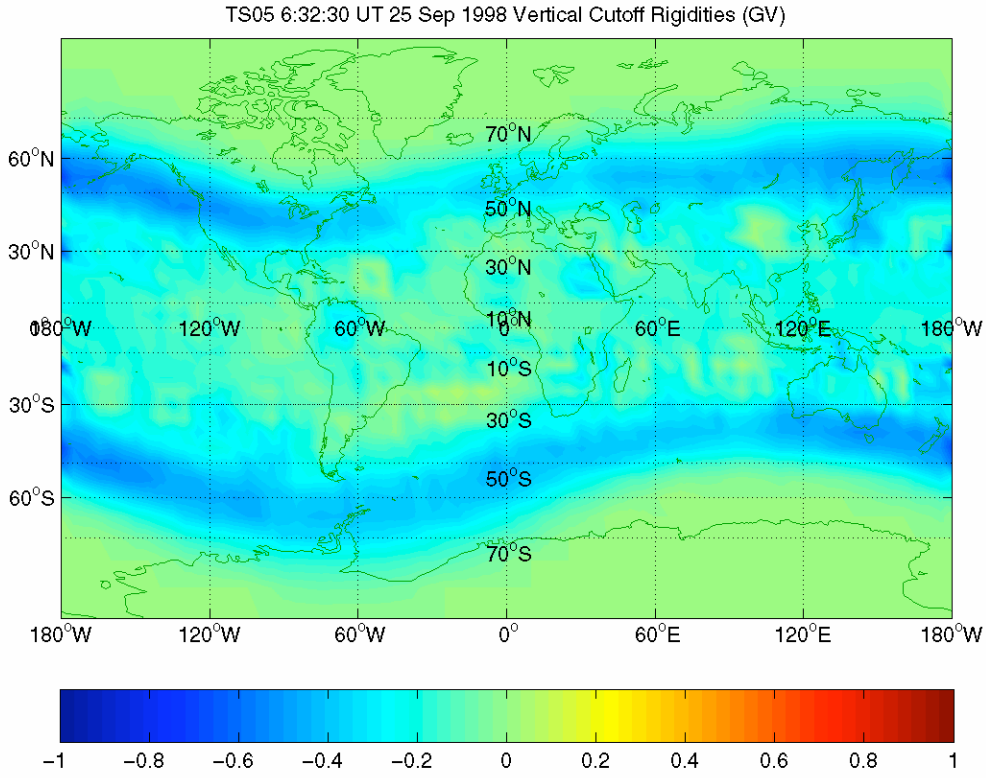

Figure 32: Storm-quiet geomagnetic cutoff rigidity (GV) computed using the T05 magnetospheric magnetic field model. The storm time snap shot corresponds to the same time as Figure 31. The quiet time snap shot corresponds to the same time as Figure 28.

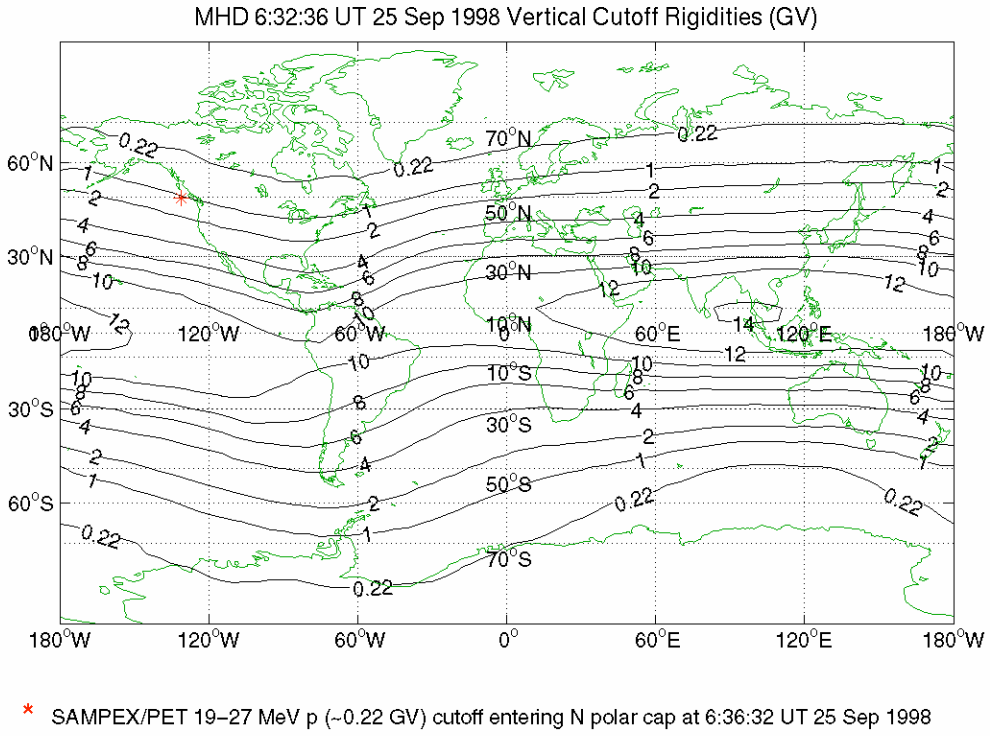

Figure 33: Same as Figure 31, except using the CMIT/LFM/MHD magnetospheric magnetic field model.

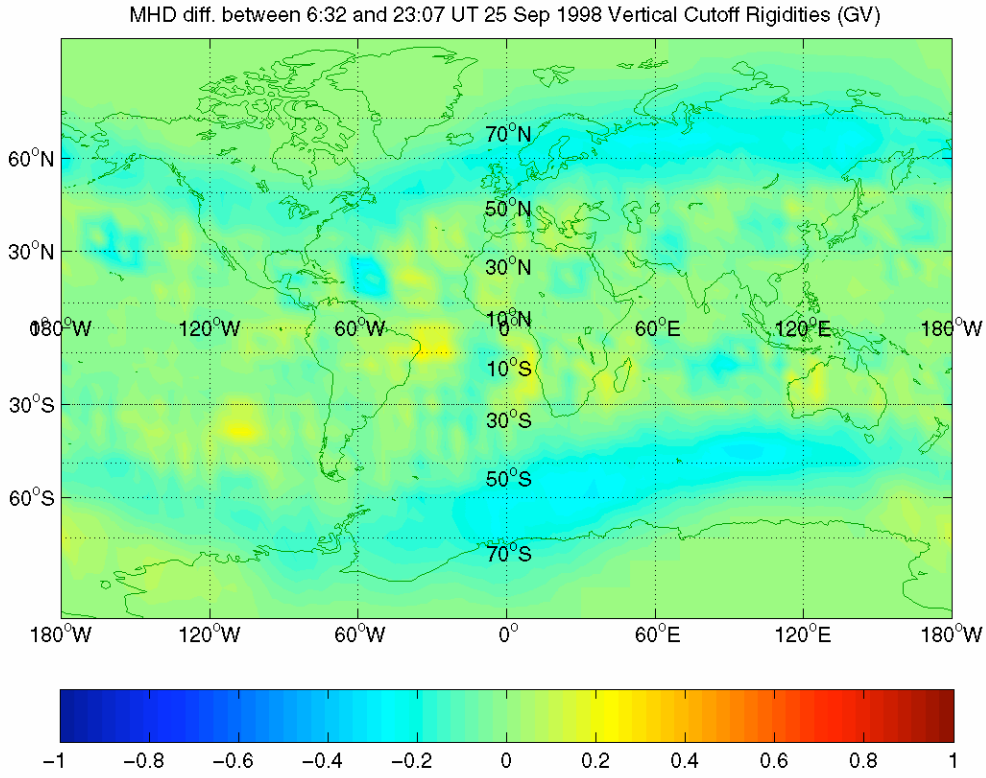

Figure 34: Same as Figure 32, except using the CMIT/LFM/MHD magnetospheric magnetic field model.